

# Revisiting Big-Bang Nucleosynthesis Constraints on Long-Lived Decaying Particles

Masahiro Kawasaki<sup>(a,b)</sup>, Kazunori Kohri<sup>(c,d)</sup>, Takeo Moroi<sup>(e,b)</sup>,  
and Yoshitaro Takaesu<sup>(e,f)</sup>

<sup>(a)</sup> *Institute for Cosmic Ray Research, The University of Tokyo, Kashiwa 277-8582, Japan*

<sup>(b)</sup> *Kavli IPMU (WPI), UTIAS, The University of Tokyo, Kashiwa 277-8583, Japan*

<sup>(c)</sup> *Theory Center, IPNS, KEK, Tsukuba 305-0801, Japan*

<sup>(d)</sup> *The Graduate University of Advanced Studies, Tsukuba 305-0801, Japan*

<sup>(e)</sup> *Department of Physics, The University of Tokyo, Tokyo 113-0033, Japan*

<sup>(f)</sup> *Research Institute for Interdisciplinary Science, Okayama University,  
Okayama 700-8530, Japan*

## Abstract

We study effects of long-lived massive particles, which decay during the big-bang nucleosynthesis (BBN) epoch, on the primordial abundances of light elements. Compared to the previous studies, (i) the reaction rates of the standard BBN reactions are updated, (ii) the most recent observational data of the light element abundances and cosmological parameters are used, (iii) the effects of the interconversion of energetic nucleons at the time of inelastic scatterings with background nuclei are considered, and (iv) the effects of the hadronic shower induced by energetic high energy anti-nucleons are included. We compare the theoretical predictions on the primordial abundances of light elements with the latest observational constraints, and derive upper bounds on the relic abundance of the decaying particle as a function of its lifetime. We also apply our analysis to unstable gravitino, the superpartner of graviton in supersymmetric theories, and obtain constraints on the reheating temperature after inflation.

# 1 Introduction

The big-bang nucleosynthesis (BBN) is one of the most important predictions of big-bang cosmology. At the cosmic temperature around 0.1 MeV, the typical energy of the cosmic microwave background (CMB) photon becomes sufficiently lower than the binding energies of the light elements (deuterium D,  $^3\text{He}$ ,  $^4\text{He}$ , and so on) so that the light elements can be synthesized with avoiding the dissociation due to the scattering with background photons. The cross sections for nuclear reactions governing the BBN are well understood so that a precise theoretical calculation of the primordial light element abundances is possible with the help of numerical calculation. In addition, the primordial abundances of the light elements are well extracted from astrophysical observations. Comparing theoretical predictions with observational constraints, a detailed test of the BBN is now possible; currently the predicted values of D and  $^4\text{He}$  in the standard BBN (SBBN) reasonably agree with observations.

It has been well recognized that, if there exists new physics beyond the standard model which may induce non-standard BBN reactions, the predictions of the SBBN change.<sup>#1</sup> In particular, with long-lived unstable particles decaying into electromagnetic [13, 14, 15, 16, 17, 18, 19, 20] or hadronic [21, 22, 23, 24, 25, 26, 27, 28, 29, 30, 31, 32] particles, the light element abundances are affected by photodissociation, hadrodissociation, and  $p \leftrightarrow n$  conversion processes. In order not to spoil the agreement between theoretical predictions and observational constraints, upper bounds on the primordial abundances of the unstable particles are obtained. Such constraints have been intensively studied in the past. Remarkably, the BBN constraints may shed light on beyond-the-standard-model particles to which collider studies cannot impose constraints. One important example is gravitino, which is the superpartner of graviton in supersymmetric (SUSY) models [33]. Gravitino is very weakly interacting, and is produced by the scattering processes of particles in the thermal bath after inflation; the primordial abundance of gravitino is approximately proportional to the reheating temperature after inflation. Consequently, with the reheating temperature being fixed, we may acquire a constraint on the gravitino mass assuming that gravitino is unstable. Such a constraint can be converted to the upper bound on the reheating temperature after inflation, which provides important information in studying cosmology based on SUSY models.

The purpose of this paper is to revisit the BBN constraints on long-lived particles, which we call  $X$ , taking into account recent progresses in theoretical and observational studies of the primordial abundances of the light elements. Theoretically, the understandings of the cross sections of the SBBN reactions have been improved, which results in smaller uncertainties in the theoretical calculations of the light element abundances. In addition, the observational constraints on the primordial abundances of the light elements have been updated. These affect the BBN constraints on the primordial abundances of long-lived particles.

In this paper, we study the BBN constraints on the primordial abundance of long-lived exotic particles, which we parameterize by using the so-called yield variable:

$$Y_X \equiv \left[ \frac{n_X}{s} \right]_{t \ll \tau_X}, \quad (1.1)$$

---

<sup>#1</sup>For earlier studies, see Refs. [1, 2, 3, 4, 5, 6, 7, 8, 9, 10, 11, 12].

where  $n_X$  is the number density of  $X$ ,  $s$  is the entropy density, and the quantity is evaluated at the cosmic time much earlier than the lifetime of  $X$  (denoted as  $\tau_X$ ). We take into account theoretical and observational progresses. In particular, compared to the previous studies:

- The reaction rates of the SBBN reactions are updated.
- The most recent observational constraints on the primordial abundances of the light elements are adopted.
- The calculation of the evolution of the hadronic showers induced by energetic nucleons from the decay is improved.
- We include the effect of hadronic shower induced by energetic anti-nucleons from the decay.<sup>#2</sup>

We consider various decay modes of long-lived particles and derive upper bounds on their abundances. We also apply our analysis to the study of the effects of unstable gravitino on the light element abundances. In the study, we adopt several patterns of mass spectra of superparticles (i.e., squarks, sleptons, gauginos, and Higgsinos) suggested by viable SUSY models, based on which the partial decay rates of gravitino are calculated.

The organization of this paper is as follows. In Section 2, we summarize the observational constraints on the light element abundances we adopt in our analysis. In Section 3, we explain how the theoretical calculation of the light element abundances is performed with taking into account the effects of the decay of long-lived particles. Upper bounds on the primordial abundances of generic decaying particles are given in Section 4. Then, our analysis is applied to the case of unstable gravitino in Section 5. Section 6 is devoted for conclusions and discussion.

## 2 Observed Abundances of the Light Elements

We first summarize the current observational constraints on the primordial abundances of the light elements D,  $^4\text{He}$ ,  $^3\text{He}$  and  $^7\text{Li}$ . In the following (A/B) denotes the ratio of number densities of light elements A and B, and the subscript “ $p$ ” indicates the primordial value.

### • D

The primordial abundance of D is inferred from D absorption in damped Ly $\alpha$  systems (DLAs). Most recently Cook *et al.* [35] measured D/H by observing a DLA toward QSO SDSS J1358+6522. Moreover they reanalyzed four previously observed DLAs and from the total five DLA data they obtained the primordial D abundance as

$$(\text{D}/\text{H})_p = (2.53 \pm 0.04) \times 10^{-5}. \quad (2.1)$$

---

<sup>#2</sup>For annihilating massive particles, we had partly considered the effects induced by anti-nucleons emitted from the annihilation [34].

The quoted error is much smaller (by a factor of  $\sim 5$ ) than those obtained in the previous study. The improvement of the D measurement is a main reason why we obtain more stringent BBN constraints than those in the previous work [28] as seen in later sections.

- **$^3\text{He}$**

The  $^3\text{He}$  abundance is measured in protosolar objects. As described in the previous work [28] we use the ratio  $^3\text{He}/\text{D}$  as observational constraint instead of using  $^3\text{He}/\text{H}$ . This is because chemical evolution can increase or decrease the  $^3\text{He}$  abundance and it is difficult to infer the primordial value for  $^3\text{He}$ . On the other hand the D abundance always decrease in chemical evolution and D is more fragile than  $^3\text{He}$ . Consequently, the ratio  $^3\text{He}/\text{D}$  increases monotonically with time, which allows us to use the measured  $^3\text{He}/\text{D}$  as an upper bound on the primordial value [36]. From  $^3\text{He}$  abundances observed in protosolar clouds [37], we adopt

$$(^3\text{He}/\text{D})_p < 0.83 + 0.27. \quad (2.2)$$

- **$^4\text{He}$**

The primordial mass fraction of  $^4\text{He}$ ,  $Y_p$ , is inferred from measurement of recombination lines of HeII (and HII) emitted from extra-galactic HII regions. Izotov, Thuan and Guseva [38] reported a new determination of  $Y_p$  with the use of the infrared as well as visible  $^4\text{He}$  emission lines in 45 extragalactic HII regions. Their result is

$$Y_p = 0.2551 \pm 0.0022. \quad (2.3)$$

After Ref. [38] was reported, Aver, Olive and Skillman [39] reanalyzed the data of Ref. [38]. They estimated the  $^4\text{He}$  abundance and its error by using Markov chain Monte Carlo (MC) analysis and obtained

$$Y_p = 0.2449 \pm 0.0040. \quad (2.4)$$

Thus, the two values are inconsistent, and the discrepancy is more than a  $2\sigma$  level. If we adopt the baryon-to-photon ratio  $\eta$  determined by Planck, the BBN prediction for  $Y_p$  is well consistent with Eq. (2.4) but not with Eq. (2.3). For this reason we adopt the value given in Eq. (2.4) as a constraint on  $Y_p$ . We will also show how constraints change if we adopt Eq. (2.3).

- **$^7\text{Li}$  (and  $^6\text{Li}$ )**

The primordial abundance of  $^7\text{Li}$  was determined by measurement of  $^7\text{Li}$  in atmospheres of old metal-poor stars. The observed  $^7\text{Li}$  abundances in stars with  $[\text{Fe}/\text{H}] = -(2.5-3)$  showed almost a constant value ( $\log_{10}(^7\text{Li}/\text{H}) \simeq -9.8$ ) called Spite plateau which was considered as primordial.<sup>#3</sup> However, the plateau value turns out to be smaller than the

---

<sup>#3</sup>  $[\text{Fe}/\text{H}] \equiv \log_{10}(\text{Fe}/\text{H}) - \log_{10}(\text{Fe}/\text{H})_{\odot}$ , where  $\odot$  indicates the solar abundance.

standard BBN prediction by a factor of nearly 3. In fact, Ref. [40] reported the plateau value  $\log_{10}(^7\text{Li}/\text{H}) = -9.801 \pm 0.086$  while the BBN prediction is  $\log_{10}(^7\text{Li}/\text{H}) = -9.35 \pm 0.06$  for the central value of  $\eta$  suggested from the CMB data [41] (see, Section 3). This discrepancy is called the lithium problem. Moreover, the recent observation shows much smaller  $^7\text{Li}$  abundances ( $\log_{10}(^7\text{Li}/\text{H}) < -10$ ) for metal-poor stars with metallicity below  $[\text{Fe}/\text{H}] \sim -3$  [40]. Thus, the situation of the  $^7\text{Li}$  observation is now controversial. Since we do not know any mechanism to make  $^7\text{Li}$  abundances small in such metal poor stars, we do not use  $^7\text{Li}$  as a constraint in this paper. We do not use  $^6\text{Li}$  either because  $^6\text{Li}$  abundance is observed as the ratio to the number density of  $^7\text{Li}$ .

### 3 BBN with Decaying Particles

In this section, we explain how we calculate the light element abundances taking into account the effects of decaying massive particles. Our procedure is based on that developed in Refs. [27, 28] with several modifications which will be explained in the following subsections.

#### 3.1 Overview

The BBN constraints strongly depend on how  $X$  decays. In order to make our discussion simple, we first concentrate on the case where  $X$  decays only into a particle and its anti-particle. The subsequent decays of the daughter particles from  $X$  decay as well as the hadronization processes of colored particles (if emitted) are studied by using the PYTHIA 8.2 package [42]. We note here that, even if  $X$  primarily decays into a pair of electromagnetically interacting particles (like  $e^+e^-$  or  $\gamma\gamma$  pair), colored particles are also emitted by the final-state radiation; such effects are included in our study.

There are two categories of the decay processes in studying the effects of long-lived particles on the BBN:

- **Radiative decay**

With the decay of the long-lived particles, high-energy photons and electromagnetically-charged particles are emitted.

- **Hadronic decay**

High-energy colored particles (i.e., quarks or gluons) are emitted in the decay.

We first overview them in the following. (A flow-chart of the effects induced by the decay of  $X$  is given in Fig. 1.)

##### 3.1.1 Radiative decay modes

Energy injections by energetic electromagnetic particles induce electromagnetic showers through their scatterings off the background photons and electrons [11, 13, 14, 15, 16, 17, 18, 26, 30, 32]. The electromagnetic particles include  $\gamma$  and  $e^\pm$  as well as charged hadrons.

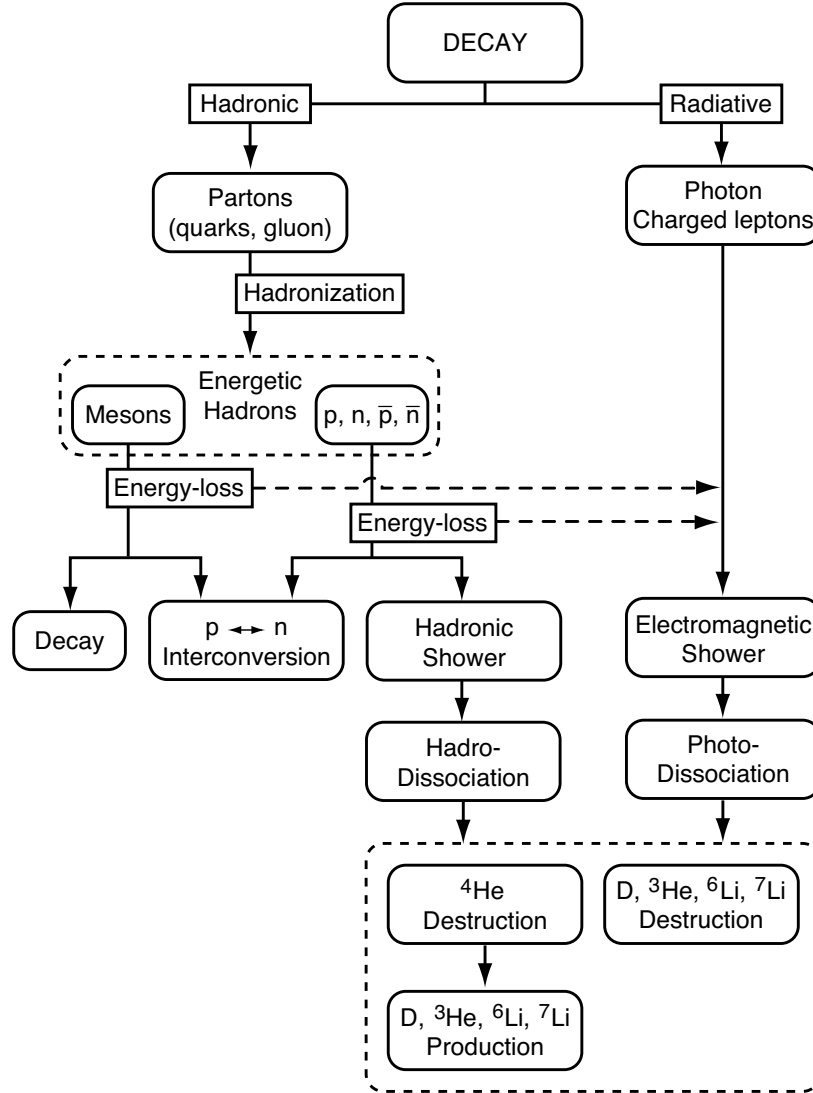


Figure 1: Flow-chart of the effects of the decay of massive particles. New effects induced by “energetic” anti-nucleons ( $\bar{n}$  and  $\bar{p}$ ) are included in this study.

Energetic photons in the shower can destroy the light elements, in particular, D and  ${}^4\text{He}$ , produced by the SBBN reactions. (Such processes are called photodissociations). The photon spectrum in the electromagnetic shower is determined by the total amount of the visible energy injected by the decay and the temperature of the background thermal bath [11, 13, 14]; in particular, at a high precision, the normalization of the photon spectrum is proportional to the total amount of the energy injection. In our numerical calculation, the total visible energy, which is the sum of the energies of photon and charged particles after the hadronization, is calculated, based on which the normalization of the photon spectrum is determined.

The photodissociation processes become effective when the threshold energy for the  $e^+e^-$

pair creation by the scattering of high energy photons and background photons, which is approximately given by  $E_{\text{th}}^{(\gamma)} \sim m_e^2/22T$  (with  $m_e$  and  $T$  being the electron mass and the cosmic temperature, respectively) [13], is larger than the threshold energy for the dissociation processes of the light elements. For the photodissociation of  ${}^4\text{He}$ , this is the case at the cosmic temperature lower than  $\sim 1$  keV (which corresponds to the cosmic time  $t \gtrsim 10^6$  sec). With the photodissociation of  ${}^4\text{He}$ , both  ${}^3\text{He}$  and D are copiously produced. Thus, for the long-lived particle with the lifetime longer than  $\sim 10^6$  sec, the D and  ${}^3\text{He}$  abundances give stringent constraints on the radiatively-decaying modes. The photodissociation of D becomes effective at higher temperature because of the smallness of its binding energy; the photodissociation of D may be important for long-lived particle with lifetime longer than  $\sim 10^4$  sec, for which significant destruction of D takes place [15, 17]. Another effect of the electromagnetic shower on BBN is non-thermal production of  ${}^6\text{Li}$ . The energetic T and  ${}^3\text{He}$  are produced through photodissociation of  ${}^4\text{He}$  and they scatter off the background  ${}^4\text{He}$  and synthesize  ${}^6\text{Li}$ . The productions of  ${}^7\text{Li}$  and  ${}^7\text{Be}$  due to energetic  ${}^4\text{He}$  scattered by energetic photons through inelastic  $\gamma + {}^4\text{He}$  are negligible.

### 3.1.2 Hadronic decay modes

In hadronic decays, the emitted colored particles fragment into hadrons such as pions, kaons, nucleons (i.e., neutron  $n$  and proton  $p$ ), and anti-nucleons (i.e., anti-neutron  $\bar{n}$  and anti-proton  $\bar{p}$ ). Hereafter,  $N = p$  or  $n$  ( $\bar{N} = \bar{p}$  or  $\bar{n}$ ) denotes the nucleon (anti-nucleon). Energetic hadrons, in particular, the nucleons, induce hadronic showers and hadrodissociation processes. (The effect of the Lorentz suppression of the decay rate is included for energetic unstable hadrons.) In addition, even after being stopped, some of the hadrons (in particular, charged pions and nucleons) change the neutron-to-proton ratio in the background plasma, which affects the  ${}^4\text{He}$  and D abundances. The most important effects of the hadronic decay modes are summarized as follows:

- When a massive particle decays into hadrons at  $T \gtrsim \mathcal{O}(0.1)$  MeV (i.e., when the lifetime is shorter than  $\sim \mathcal{O}(10^2)$  sec), the high-energy hadrons are stopped in the thermal plasma [28]. The extra pions and nucleons affect the neutron-to-proton ratio after the neutron freeze-out by interchanging background  $p$  and  $n$  through the strongly-interacting interconversion processes like

$$\pi^+ + n \longrightarrow p + \pi^0, \quad (3.1)$$

$$\pi^- + p \longrightarrow n + \pi^0. \quad (3.2)$$

There also exist similar interconversion processes caused by the injected nucleons. The neutron-to-proton ratio  $n/p$  increases due to the strongly-interacting conversions, resulting in the increase of the abundances of  ${}^4\text{He}$  and D [21, 25].

- If the background temperature at the time of the decay is low enough, the emitted hadrons cannot be stopped in the plasma; this is the case for energetic  $n$  and  $\bar{n}$  ( $p$  and  $\bar{p}$ ) if  $T \lesssim 0.1$  MeV ( $T \lesssim 30$  keV) [28]. The energetic nucleons scatter off and destroy the

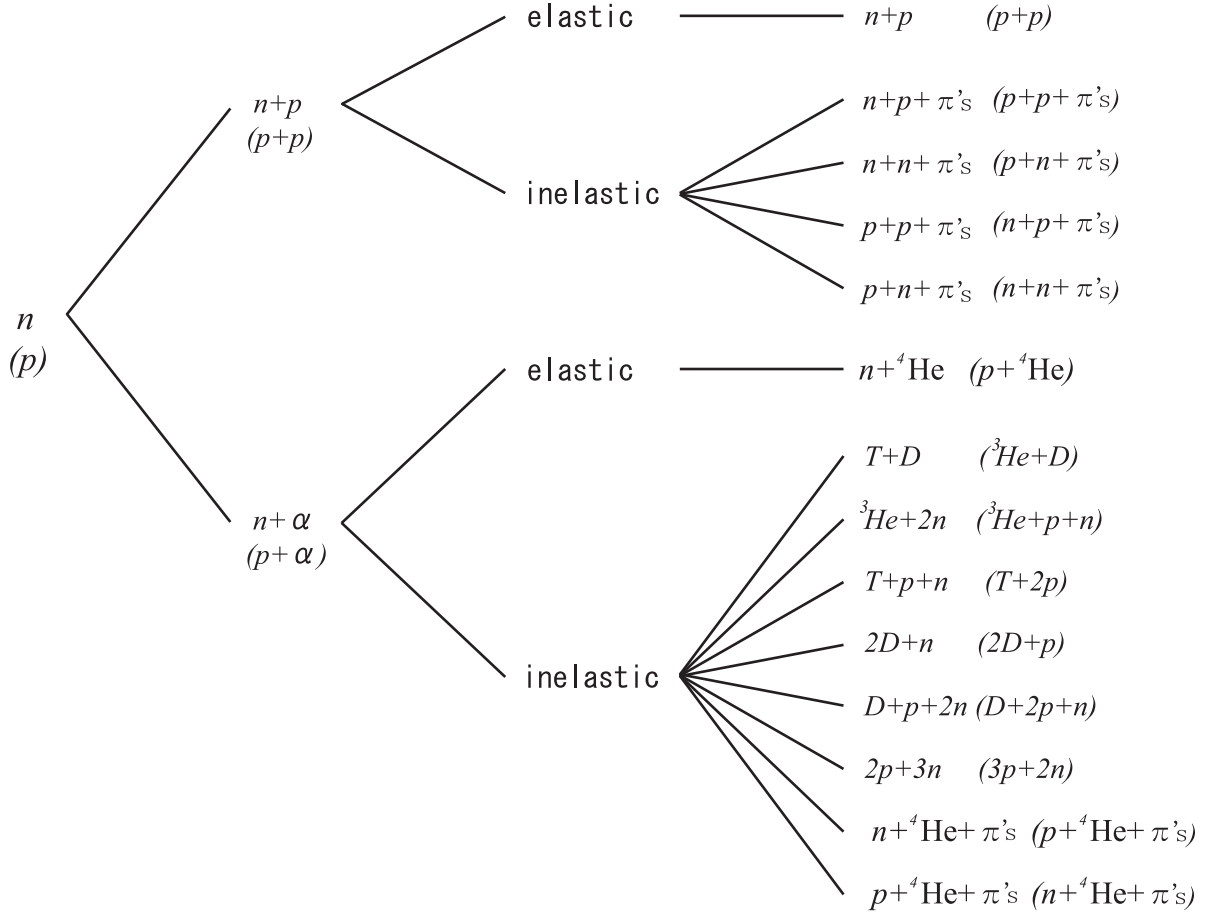


Figure 2: Schematic picture of hadronic shower induced by a high energy projectile  $n$  (or  $p$ ) which scatters off the background proton or the background  ${}^4\text{He}$ . (Here  $T$  denotes tritium.)

background nuclei [22, 23, 24]. The processes considered in this study are summarized in Figs. 2 and 3. In particular, through the destruction of  ${}^4\text{He}$  by the high-energy neutrons, an overproduction of D may occur, which leads to a stringent constraint on the primordial abundance of the hadronically decaying long-lived particles [27, 28, 31, 34]. In addition, energetic  ${}^3\text{He}$ ,  ${}^4\text{He}$  and T produce  ${}^7\text{Li}$ ,  ${}^7\text{Be}$  and  ${}^6\text{Li}$  non-thermally through scattering off the background  ${}^4\text{He}$ .

### 3.2 New implementations in the numerical calculation

As mentioned before, our analysis is based on Refs. [27, 28]. Here, we summarize the new implementations in the numerical calculation added after Refs. [27, 28, 31].

- We update the SBBN reaction rates and their uncertainties.

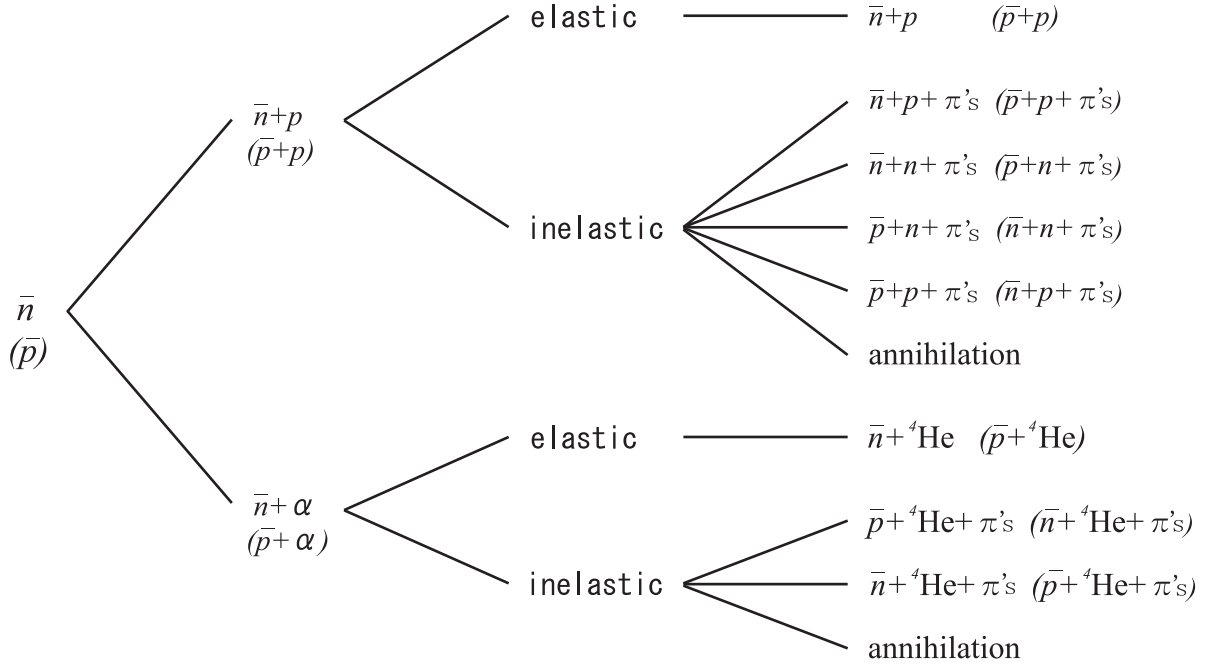


Figure 3: Same as Fig. 2, but for a high energy projectile  $\bar{n}$  (or  $\bar{p}$ ).

- We revise the algorithm to calculate the evolution of the hadronic shower induced by the injections of energetic  $p$  and  $n$ . In particular, we include the  $p \leftrightarrow n$  interconversion of the energetic nucleons via inelastic scatterings.<sup>#4</sup> In the inelastic scattering processes of energetic nucleon (i.e.,  $p$ ,  $n$ ,  $\bar{p}$ , or  $\bar{n}$ ) with the background nuclei, it is likely that the projectile nucleon carries away most of the energy while other final state particles are less energetic; the kinetic energies of the final-state particles other than the most energetic one are typically  $K_T \sim 140$  MeV. The conversion of the projectile nucleon via the inelastic scatterings affects the (effective) energy loss rate of the nucleon as we discuss below.
- We newly include the effects of energetic  $\bar{p}$  and  $\bar{n}$  injections by the decay.

### 3.2.1 SBBN reactions

Compared to the previous studies [28, 31], we update the SBBN reaction rates adopting those given in Ref. [43, 44], which are obtained by fitting relatively-new experimental data. In order to take into account uncertainties in the reaction rates, we perform MC simulations

<sup>#4</sup>The interconversions of energetic  $p$  and  $n$  should not be confused with the interconversions of background  $p$  and  $n$ . The former affects the stopping rate of the energetic nucleons which induces hadronic showers as well as hadrodissociation processes. On the contrary, the latter affects the neutron-to-proton ratio after the neutron freeze-out to which  $Y_p$  is sensitive; the effects of the latter has been already taken into account in the previous analysis [25, 27, 28, 31].

to estimate error propagations to the light element abundances. For given values of the lifetime and the primordial abundance of  $X$ , we perform 1,000 runs of the calculation of the light element abundances with assuming that the reaction rates (as well as other parameters in the calculation) are random Gaussian variables. In each run, the reaction rate  $R_i$  for  $i$ -th reaction is determined as

$$R_i(T) = \bar{R}_i(T) + \sigma_i(T) y_i, \quad (3.3)$$

where  $\bar{R}_i$  and  $\sigma_i$  are the central value and the standard deviation of the reaction  $i$ , and  $y_i$  is the temperature independent Gaussian variable with probability distribution

$$P(y) = \frac{1}{\sqrt{2\pi}} \exp\left(-\frac{1}{2}y^2\right). \quad (3.4)$$

Notice that, as explicitly shown in Eq. (3.3), some of uncertainties of reaction rates depend on the cosmic temperature. Throughout each run, such a reaction rate is determined by adding the temperature-dependent uncertainty multiplied by the temperature-independent random Gaussian variable to the central value. If the upper and lower uncertainties of a reaction rate are asymmetric, we take upward and downward fluctuations with equal probability, assuming that they obey one-sided Gaussian distributions.

In order to check the consistency between the observational constraints summarized in Section 2 and the SBBN predictions, we compare them in Fig. 4; we plot the SBBN values of the light element abundances as functions of the baryon to photon ratio  $\eta = n_B/n_\gamma$ . From the top to the bottom, we plot (i) the mass fraction of  $^4\text{He}$  ( $Y_p$ ), (ii) the deuterium to hydrogen ratio (D/H), (iii) the  $^3\text{He}$  to hydrogen ratio ( $^3\text{He}/\text{H}$ ), (iv) the  $^7\text{Li}$  to hydrogen ratio ( $^7\text{Li}/\text{H}$ ), and (v) the helium 3 to deuterium ratio ( $^3\text{He}/\text{D}$ ). The theoretical predictions show  $2\sigma$  bands due to the uncertainties in experimental data of cross sections and lifetimes of nuclei. The boxes indicate the  $2\sigma$  observational constraints (see Section 2). The CMB observations provide independent information about the baryon-to-photon ratio; we adopt

$$\eta = (6.11 \pm 0.04) \times 10^{-10} \quad (68\% \text{ C.L.}), \quad (3.5)$$

which is based on the TT,TE,EE+lowP+BAO analysis of the Planck collaboration,  $\Omega_B h^2 = 0.02229_{-0.00027}^{+0.00029}$  (95% C.L.), where  $\Omega_B$  is the density parameter of baryon and  $h$  is the Hubble constant in units of 100 km/sec/Mpc [41]. In Fig. 4, we also show the CMB constraint on  $\eta$  at  $2\sigma$  (the vertical band). We can see that the SBBN predictions based on the baryon-to-photon ratio suggested from the CMB observations are in reasonable agreements with observations.

### 3.2.2 High energy $n$ and $p$ injections

The effects of the high energy  $n$  and  $p$  injected into the thermal bath have been studied in Refs. [22, 23, 24, 27, 28]. Compared to the previous studies, we newly include the interconversion reactions between energetic  $p$  and  $n$  at the time of the inelastic scatterings accompanied by pion emissions (see Fig. 2). Once an energetic  $p$  or  $n$  is injected into thermal plasma, it can be converted to  $n$  or  $p$  through inelastic scatterings off the background nuclei, i.e.,  $p$

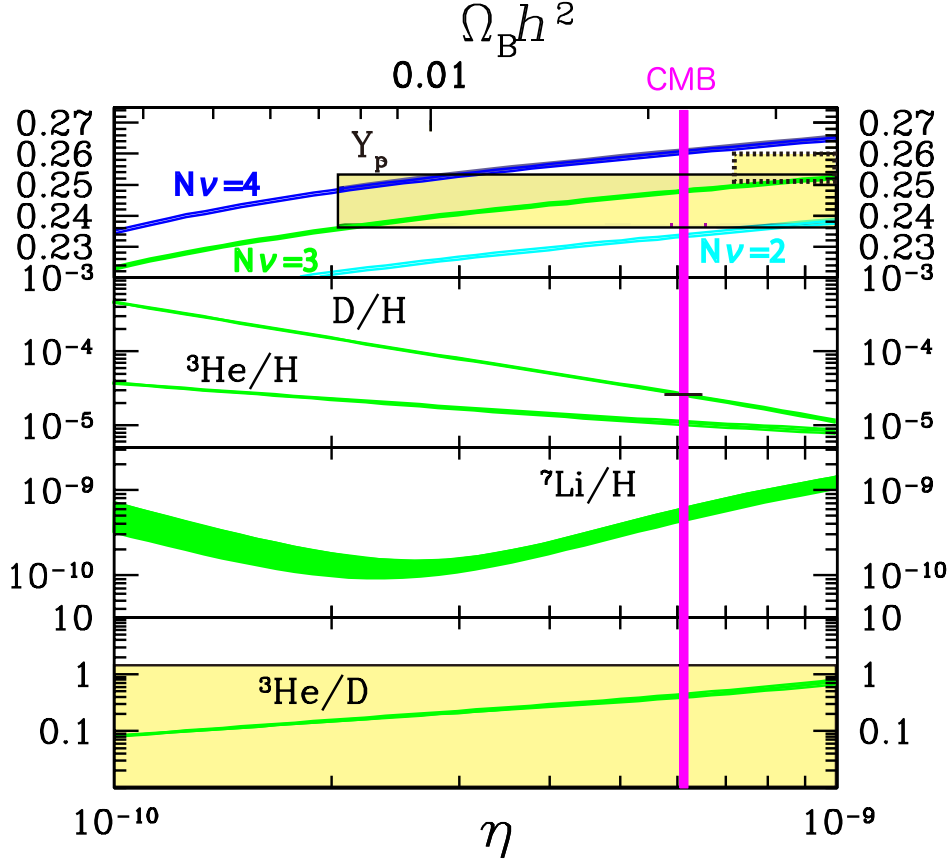


Figure 4: Theoretical predictions of the light element abundances as functions of the baryon-to-photon ratio  $\eta = n_B/n_\gamma$ . (The upper horizontal axis shows  $\Omega_B h^2$ , where  $\Omega_B$  is the density parameter of baryon and  $h$  is the Hubble constant in units of 100 km/sec/Mpc.) The vertical band shows  $\eta = (6.11 \pm 0.08) \times 10^{-10}$ , which is the  $2\sigma$  band of baryon-to-photon ratio suggested by the CMB observations [41]. For  $Y_p$ , we plot results for effective number of neutrino species  $N_\nu = 2, 3$ , and 4 (from the bottom to the top). The boxes indicate the observational values with  $2\sigma$  uncertainties. (For  $Y_p$ , the box surrounded by the solid and dashed lines correspond to Eq. (2.4) and Eq. (2.3), respectively.)

or  ${}^4\text{He}$ . (Hereafter, the background  ${}^4\text{He}$  is denoted as  $\alpha_{\text{BG}}$ .) As we discuss below, such an interconversion affects the (effective) energy loss rates of nucleons during their propagation in thermal plasma, resulting in a change of the hadrodissociation rates.

The effects of the interconversions of energetic  $p$  and  $n$  are important when the cosmic temperature becomes lower than  $\sim 0.1$  MeV. This is because the energetic nucleons are stopped in the thermal plasma if the background temperature is high enough; as we have mentioned, the neutron is likely to be stopped when  $T \gtrsim 0.1$  MeV while the proton is stopped when  $T \gtrsim 30$  keV. Once stopped, the nucleons do not induce hadrodissociation processes. An energetic neutron, which would have a sufficient time to induce hadronic showers without the interconversion, does not cause hadronic showers when it is converted to proton. Thus, the inclusion of the energetic  $p \leftrightarrow n$  conversion makes the BBN constraints milder in particular when  $30 \text{ keV} \lesssim T \lesssim 0.1 \text{ MeV}$  (i.e.,  $10^2 \text{ sec} \lesssim t \lesssim 10^3 \text{ sec}$ ). The inelastic scatterings occur with the targets of  $p$  and  $\alpha_{\text{BG}}$ . The interconversion rates are estimated as follows:

- Because of the lack of the experimental data of a cross section of each mode for the  $n$  (projectile)+  $p$  (target) and  $p$  (projectile)+  $p$  (target) processes shown in Fig. 2, we assume that all of the cross sections for those 8 modes ( $n+p$ ,  $p+p \rightarrow p+p+\pi$ 's,  $p+n+\pi$ 's,  $n+p+\pi$ 's,  $n+n+\pi$ 's) are equal. (In the case of  $p+p \rightarrow n+n+\pi$ 's, at least two pions should be emitted and hence we consider the process only if it is kinematically allowed.) In addition, we neglect the effects of the interconversions induced by the emitted pions from the inelastic scatterings. That is because those pions decay before they scatter off the background particles.
- With inelastic  $n+\alpha_{\text{BG}}$  scatterings, the energetic  $n$  can be again converted to  $p$ . Because of the lack of experimental data, we assume that, when the inelastic processes with pion emissions are concerned, the cross section for  $n+{}^4\text{He}$  scattering is equal to that for  $p+{}^4\text{He}$  scattering. Since the rates of the inelastic scatterings  $n+{}^4\text{He} \rightarrow n+{}^4\text{He}$  and  $p+{}^4\text{He}$  are relatively small [45], effects of the interconversion due to the inelastic  $n+\alpha_{\text{BG}}$  scatterings are unimportant and does not change the hadronic shower evolution.

We also comment on the non-thermal production processes of  ${}^6\text{Li}$ ,  ${}^7\text{Li}$ , and  ${}^7\text{Be}$ . With the inelastic scatterings  $N + \alpha_{\text{BG}} \rightarrow \dots$ , the final state may contain energetic T,  ${}^3\text{He}$ , and  ${}^4\text{He}$ . They may scatter off  $\alpha_{\text{BG}}$  to produce heavier elements, i.e.,  ${}^6\text{Li}$ ,  ${}^7\text{Li}$ , and  ${}^7\text{Be}$  [22, 23, 24, 28]. Although we do not use  ${}^6\text{Li}$  and  ${}^7\text{Li}$  to constrain the primordial abundance of  $X$ , these non-thermal production processes are included in our numerical calculation. In particular, we include the processes  ${}^4\text{He} + \alpha_{\text{BG}} \rightarrow {}^6\text{Li} + \dots$ ,  ${}^7\text{Li} + \dots$ , and  ${}^7\text{Be} + \dots$ , whose effects were not taken into account in Ref. [28]. For the study of these processes, energy distribution of  ${}^4\text{He}$  produced by the inelastic hadronic scatterings is necessary. We determine energy distribution of the final-state  ${}^4\text{He}$  using the prescription given in Appendix C of Ref. [28]. Notice that, for the non-thermal production processes of  ${}^6\text{Li}$  induced by T and  ${}^3\text{He}$ , the energy distributions of T and  ${}^3\text{He}$  produced by the hadrodissociations of  $\alpha_{\text{BG}}$  are obtained by fitting experimental data (see Ref. [28]).

### 3.2.3 Injections of energetic $\bar{n}$ or $\bar{p}$

In the present study, we newly include the effects of the injections of energetic anti-nucleons,  $\bar{n}$  or  $\bar{p}$ . We only consider the scatterings of energetic anti-nucleons off the background  $p$  and  $\alpha_{\text{BG}}$ , and the anti-nucleons are treated as sources of hadronic showers.<sup>#5</sup> The high-energy nucleons in the hadronic showers induced by  $\bar{n}$  and  $\bar{p}$  can destroy  $\alpha_{\text{BG}}$  and further produce copious high-energy daughter nuclei. In Fig. 3, we show a schematic picture for the reactions induced by energetic anti-nucleons. Because of the lack of experimental data for the processes including the anti-nucleons, we adopt several approximations and assumptions on the reactions induced by the energetic anti-nucleon. We note here that, in adopting approximations or assumptions, we require that the constraints become conservative in order not to over-constrain the properties of long-lived particles.

First, let us consider the scattering of energetic anti-nucleons with the background  $p$ . We use the experimental data of the differential cross sections for the  $\bar{p}$ - $p$  scatterings by referring Ref. [46] for the total and elastic cross sections and Ref. [47] for the annihilation cross sections. Because of the lack of experimental data, we use the data for the  $\bar{p}$ - $p$  scatterings to estimate the cross sections for other processes. (i) We assume that the differential cross sections for  $\bar{n}$ - $p$  scatterings are the same as those of corresponding  $\bar{p}$ - $p$  scatterings paired in Fig. 3. We expect that this assumption is reasonable because the Coulomb corrections to the cross sections are estimated to be less than a few percent for the energy of our interest [28]. (ii) Through inelastic scatterings off the background  $p$ , the strongly-interacting  $p \leftrightarrow n$  interconversion reactions occur with emitting pions. Then, there are four possible combinations of final-state anti-nucleon and scattered nucleon; the final-state anti-nucleon may be  $\bar{p}$  or  $\bar{n}$ , while the nucleon may be  $p$  or  $n$  (see Fig. 3). We assume that the differential cross sections for these processes are equal and use the data for the  $\bar{p}$ - $p$  scatterings for all of these processes because the cross sections for some of the final states are unknown. Here one remark is that the process  $\bar{n}(\text{projectile}) + p(\text{target}) \rightarrow \bar{p} + n$  needs at least two pion emission so we take into account it if kinematically allowed.

Next, we discuss scatterings of energetic anti-nucleons off  $\alpha_{\text{BG}}$ . Unfortunately, experimental data of the cross sections for the scattering processes of anti-nucleon with  ${}^4\text{He}$  are insufficient to perform a detailed study. Therefore, we only consider the energy-loss and interconversions of anti-nucleon induced by the inelastic scatterings with  $\alpha_{\text{BG}}$ . Approximating that the energetic anti-nucleon scatters off individual nucleons in  ${}^4\text{He}$ , the cross sections for the scattering processes with  ${}^4\text{He}$  are taken to be four times larger than those with the background nucleons. Notice that this assumption is reasonable when the energy of  $\bar{N}$  is larger than the binding energy of  ${}^4\text{He}$ .<sup>#6</sup> In addition, for the scatterings induced by the anti-nucleon, we neglect the subsequent reactions induced by the cascade products from  $\alpha_{\text{BG}}$ ; in other words, we neglect the destruction of  $\alpha_{\text{BG}}$  and the recoil energy of  $\alpha_{\text{BG}}$  (if it is not

<sup>#5</sup>On the other hand, for anti-nucleons stopped in the plasma, we have already explained their effects on the inter-conversion reactions between background  $n$  and  $p$  in previous subsections.

<sup>#6</sup>For example, see the plots shown in Ref. [46] in which the cross section of the process  $\bar{p} + \text{D}$  is approximately twice larger than that of  $\bar{p} + n$  for a high-energy  $\bar{p}$ . Similarly, it is also known that the cross sections of  $\bar{p} + {}^4\text{He}$  are approximately four times larger than that of  $\bar{p} + n$  at high energies.

destroyed). These would give the most conservative bounds.

For annihilation reactions of anti-nucleon with background  $p$  or  $\alpha_{\text{BG}}$ , we expect emissions of energetic hadrons, by which the light element abundances should be affected. However, because we do not have sufficient data of differential cross sections, we conservatively neglect any effects after the annihilation of anti-nucleon. Thus, in our calculation, only the effect of the pair annihilations of anti-nucleon is to reduce the number of energetic anti-nucleon.

### 3.2.4 $\xi$ parameters

In the present study, the effects of the hadrodissociation are parameterized by the functions called  $\xi_{A_i}$  (with  $A_i$  being  $n$ , D, T,  ${}^3\text{He}$ ,  $\alpha$ ,  ${}^6\text{Li}$ ,  ${}^7\text{Li}$  and  ${}^7\text{Be}$ ) [22, 23, 24, 27, 28]. For  $A_i \neq \alpha$ ,  $\xi_{A_i}$  is the total number of  $A_i$  produced by the hadronic decay of one parent particle  $X$ , while  $\xi_\alpha$  is the total number of  $\alpha_{\text{BG}}$  destroyed. With the properties of the long-lived particle  $X$  being given,  $\xi_{A_i}$  depend on three quantities: the cosmic temperature  $T$ , the mass fraction of  ${}^4\text{He}$ , and the baryon-to-photon ratio  $\eta$ .

It is notable that  $\xi_{A_i}$  is defined as the value just after the shower evolutions. Notice that the timescale of the shower evolution is much shorter than those of any nuclear reactions in SBBN. Therefore, the face value of  $\xi_{A_i}$  does not represent a net increase or decrease of the nuclei  $A_i$ . For example,  ${}^6\text{Li}$  produced by the non-thermal reactions may be further processed in the SBBN reaction as  ${}^6\text{Li} + p \rightarrow {}^3\text{He} + {}^4\text{He}$ .

In the case of our interest, the hadronic showers are triggered by the injections of high-energy nucleons (i.e.,  $N = p$  and  $n$ ) and anti-nucleons (i.e.,  $\bar{N} = \bar{p}$  and  $\bar{n}$ ) which originate from the hadronizations of colored particles emitted by the decay of long-lived particles.  $\xi_{A_i}$  are given by the convolutions of two functions as

$$\xi_{A_i}(T, Y_p, \eta) = \sum_{N=n, \bar{n}, p, \bar{p}} \int \tilde{\xi}_{A_i, N}(E_N, T, Y_p, \eta) \frac{dn_N}{dE_N} dE_N, \quad (3.6)$$

where  $(dn_N/dE_N)$  is the energy spectrum of the injected nucleon  $N$  with energy  $E_N$  per a single massive particle decay, while  $\tilde{\xi}_{A_i, N}$  is the number of the light element  $A_i$  produced (or destroyed for  $A_i = \alpha$ ) by the products of hadronic shower induced by the injection of single  $N$  with energy  $E_N$ . We calculate the functions  $\tilde{\xi}_{A_i, N}$  based on the procedure explained in Ref. [28].<sup>#7</sup>

In Figs. 5, 6, 7, 8 and 9, we show  $\tilde{\xi}_{n, N}$ ,  $\tilde{\xi}_{\text{D}, N}$ ,  $\tilde{\xi}_{\text{T}, N}$ ,  $\tilde{\xi}_{{}^3\text{He}, N}$ , and  $\tilde{\xi}_{\alpha, N}$ , respectively, as functions of the kinetic energy  $E_N$  for  $N = n, \bar{n}, p$  and  $\bar{p}$ , taking  $T = 4$  keV. Notice that, at  $T = 4$  keV, the energetic neutrons with  $E_n > \mathcal{O}(1)$  TeV lose their kinetic energy immediately down to  $\sim 1$  TeV [31]. Thus,  $\tilde{\xi}_{\alpha, N}$  become insensitive to  $E_N$  for  $E_N \gtrsim 1$  TeV. On the same token, the emitted high-energy protons with  $E_n > \mathcal{O}(10)$  GeV lose their kinetic

<sup>#7</sup>In the calculation of  $\xi_{{}^6\text{Li}}$  in Ref. [28], there was an error in numerical calculation of the Coulomb stopping powers of energetic T and  ${}^3\text{He}$ , with which  $\xi_{{}^6\text{Li}}$  was maximized at the cosmic temperature of  $\sim 40 - 50$  keV. The error was corrected in subsequent studies, e.g., in Ref. [48], and  $\xi_{{}^6\text{Li}}$  is peaked at the cosmic temperature of  $T \sim 20$  keV. However, the error did not affect the resultant value of relic  ${}^6\text{Li}$  abundance because  ${}^6\text{Li}$ , if it exists, is completely destroyed by the process of  ${}^6\text{Li} + p \rightarrow {}^3\text{He} + {}^4\text{He}$ . We thank K. Jedamzik for his comments on this issue.

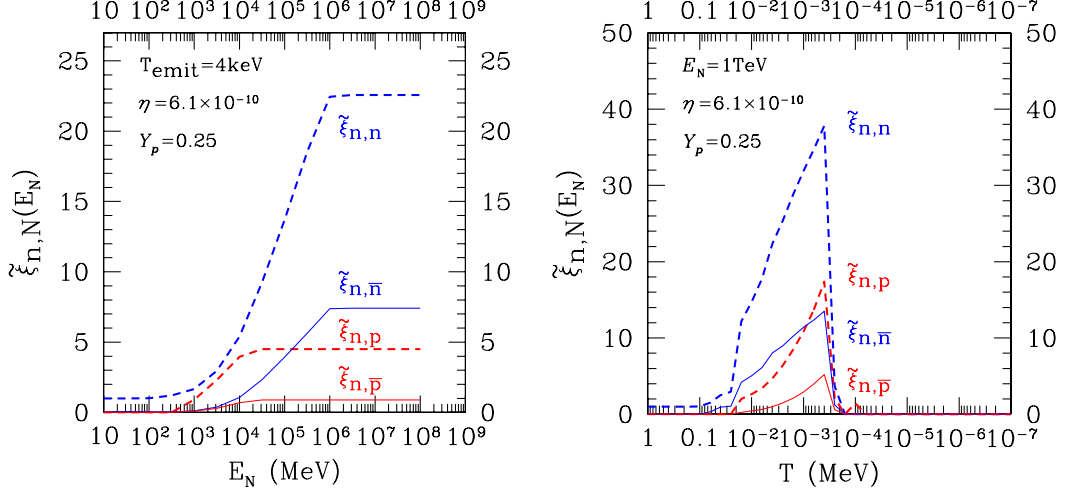


Figure 5:  $\tilde{\xi}_{n,N}$  for  $T = 4$  keV as functions of the kinetic energy (left) and those for  $E_N = 1$  TeV as functions of the cosmic temperature (right). Here,  $N = n, \bar{n}, p$  and  $\bar{p}$ , and we take  $\eta = 6.1 \times 10^{-10}$  and  $Y_p = 0.25$ .

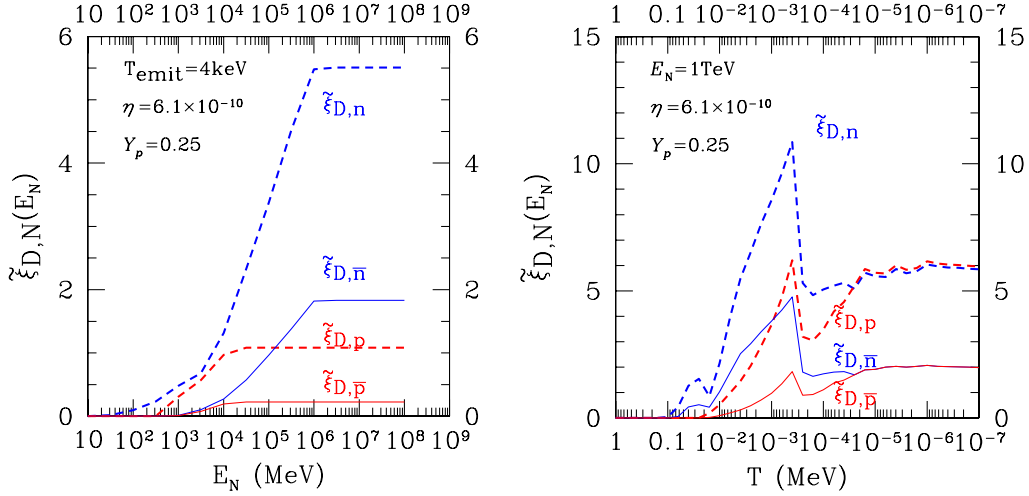


Figure 6:  $\tilde{\xi}_{D,N}$  for  $T = 4$  keV as functions of the kinetic energy (left) and those for  $E_N = 1$  TeV as functions of the cosmic temperature (right). Here,  $N = n, \bar{n}, p$  and  $\bar{p}$ , and we take  $\eta = 6.1 \times 10^{-10}$  and  $Y_p = 0.25$ .

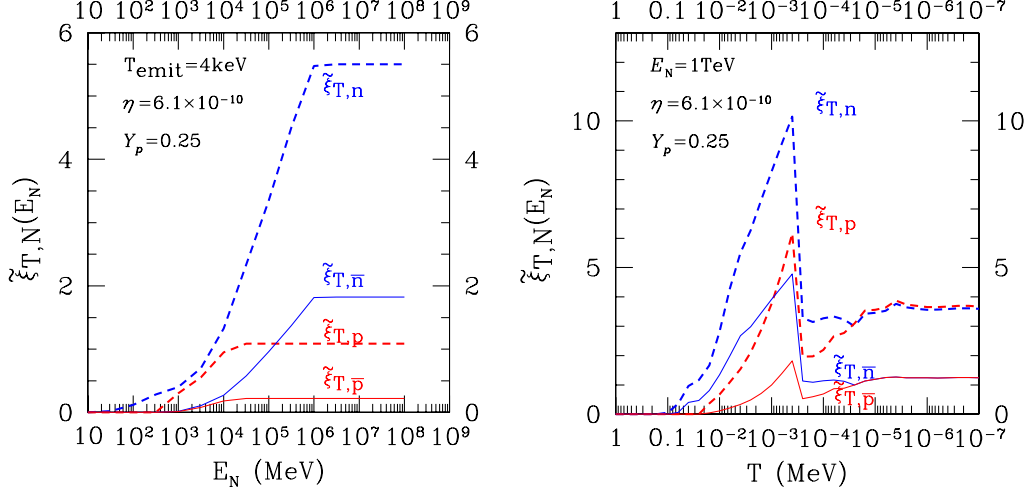


Figure 7:  $\tilde{\xi}_{T,N}$  for  $T = 4$  keV as functions of the kinetic energy (left) and those for  $E_N = 1$  TeV as functions of the cosmic temperature (right). (In the subscript of  $\tilde{\xi}_{T,N}$ ,  $T$  denotes tritium.) Here,  $N = n, \bar{n}, p$  and  $\bar{p}$ , and we take  $\eta = 6.1 \times 10^{-10}$  and  $Y_p = 0.25$ .

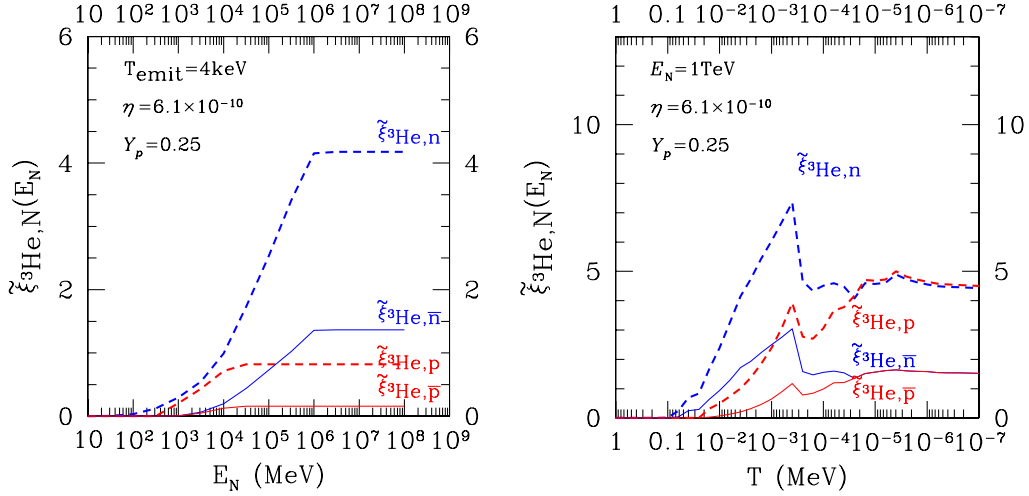


Figure 8:  $\tilde{\xi}_{^3\text{He},N}$  for  $T = 4$  keV as functions of the kinetic energy (left) and those for  $E_N = 1$  TeV as functions of the cosmic temperature (right). Here,  $N = n, \bar{n}, p$  and  $\bar{p}$ , and we take  $\eta = 6.1 \times 10^{-10}$  and  $Y_p = 0.25$ .

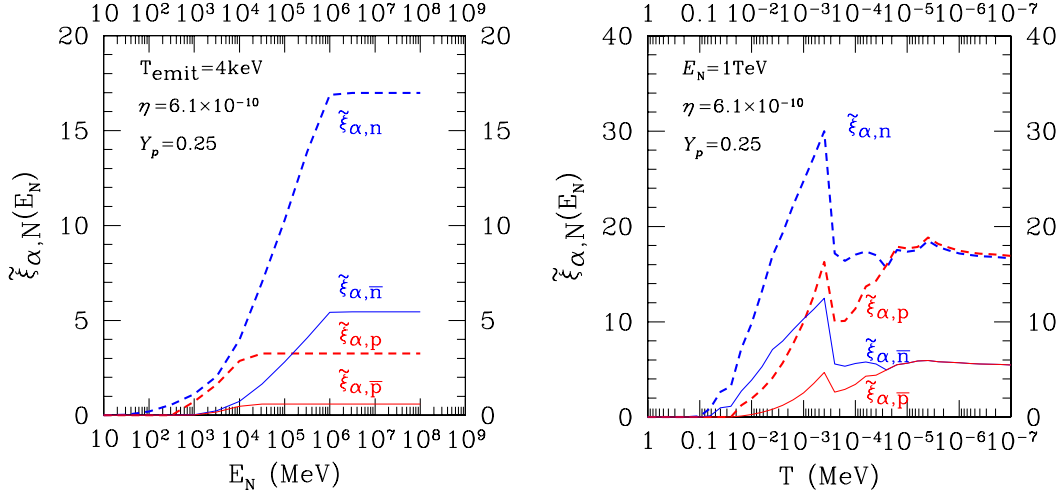


Figure 9:  $\tilde{\xi}_{\alpha,N}$  for  $T = 4 \text{ keV}$  as functions of the kinetic energy (left) and those for  $E_N = 1 \text{ TeV}$  as functions of the cosmic temperature (right). Here,  $N = n, \bar{n}, p$  and  $\bar{p}$ , and we take  $\eta = 6.1 \times 10^{-10}$  and  $Y_p = 0.25$ .

energy down to  $\sim 10 \text{ GeV}$ . The figures also show how the  $\tilde{\xi}_{A_i,N}$  parameters depend on the cosmic temperature, taking  $E_N = 1 \text{ TeV}$ . As one can see,  $\tilde{\xi}_{A_i,N}$  parameters increase as the temperature decreases until  $T \sim 0.5 \text{ keV}$ ; this is because the mean free paths of energetic nucleons become longer as the temperature drops. We can also see sharp drop-offs of the  $\tilde{\xi}$ -parameters at  $T \sim 0.5 \text{ keV}$ ; they come from the fact that, when the cosmic temperature is lower than  $\sim 0.5 \text{ keV}$ , the energetic neutrons decay before scattering off the background nuclei and that the neutron contributions to the hadrodissociations become negligible.

From the figures, we find that the injections of  $\bar{n}$  and  $\bar{p}$  should change the total number of the destroyed  $\alpha_{\text{BG}}$  by  $\sim 20 - 30 \%$ . As will be shown later, the constraints become stronger by  $10 - 30 \%$  when we include the hadrodissociations by anti-nucleons. On the other hand, by the effects of the interconversions at inelastic scatterings, the constraints become weaker by  $50 - 80 \%$ . That is because the high-energy protons which can be produced by interconversion from a projectile neutron tend to be stopped more easily than neutrons through electromagnetic interactions inside the thermal plasma.

For comparison, in Fig. 10, we plot  $\tilde{\xi}_{\alpha,N}$  based on the current method as well as those based on the old method [28] which is without the interconversions between  $n$  and  $p$  at inelastic scattering. We can see that the current  $\tilde{\xi}_{\alpha,n}$  is reduced to about a half of the old one because neutrons are converted to protons during the hadronic shower evolutions. (Notice that protons are stopped more easily than neutrons.) On the other hand the current  $\tilde{\xi}_{\alpha,p}$  is larger than the old one because of the conversion from protons to neutrons.

With  $\xi_{A_i}(T, Y_p, \eta)$  being given, the effects of the hadrodissociation are included into the Boltzmann equations which govern the evolutions of the light element abundances; for

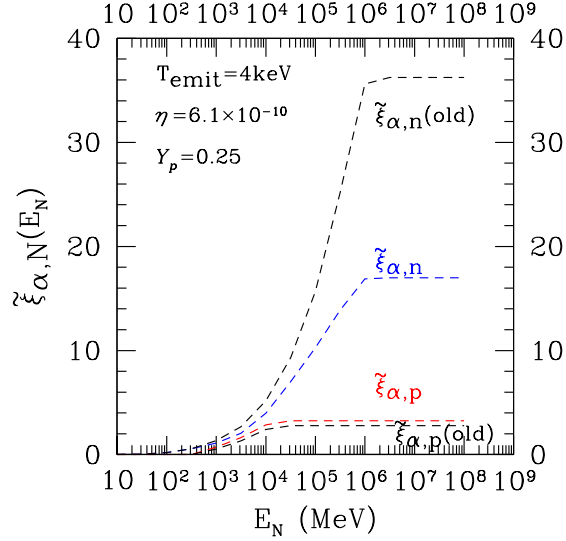


Figure 10:  $\tilde{\xi}_{\alpha,N}$  for  $T = 4$  keV as functions of the kinetic energy, based on the current method (red and blue) as well as those based on the old method which is without the interconversions between  $n$  and  $p$  at inelastic scattering (black). Here, we take the same parameters as those used in the left panel of Fig. 9.

$A_i = n, T, D, {}^3\text{He}$ , we use

$$\frac{dn_{A_i}}{dt} = \left[ \frac{dn_{A_i}}{dt} \right]_{\text{SBBN}} + \left[ \frac{dn_{A_i}}{dt} \right]_{\text{photodis}} + n_X \Gamma_X \xi_{A_i}, \quad (3.7)$$

while

$$\frac{dn_{{}^4\text{He}}}{dt} = \left[ \frac{dn_{{}^4\text{He}}}{dt} \right]_{\text{SBBN}} + \left[ \frac{dn_{{}^4\text{He}}}{dt} \right]_{\text{photodis}} - n_X \Gamma_X \xi_{\alpha}. \quad (3.8)$$

Here, the subscript ‘‘SBBN’’ and ‘‘photodis’’ imply the reaction rates due to the SBBN and photodissociation processes. Notice that the effects of the  $p \leftrightarrow n$  interconversions of the background nucleons are included in the SBBN contributions by properly modifying the number densities of the background  $p$  and  $n$ .

For  ${}^6\text{Li}$ ,  ${}^7\text{Li}$  and  ${}^7\text{Be}$ , we include non-thermal production processes induced by secondary energetic  $T$ ,  ${}^3\text{He}$ ,  ${}^4\text{He}$ . Such energetic nuclei are produced by the hadronic scatterings of energetic nucleons off the background  $\alpha_{\text{BG}}$  as well as by the electromagnetic processes of energetic photons. For the non-thermal processes induced by hadrons, the effects are pa-

parameterized by the following quantity (with  $A_f = {}^6\text{Li}$ ,  ${}^7\text{Li}$  and  ${}^7\text{Be}$ ) [22, 23, 24, 28]

$$\xi_{A_f} = \sum_{A_i=\text{T}, {}^3\text{He}, {}^4\text{He}} \int dE_{A_i}^{(\text{in})} f_{A_i}(E_{A_i}^{(\text{in})}) \int^{E_{A_i}^{(\text{in})}} dE_{A_i} \left( \frac{dE_{A_i}}{dt} \right)^{-1} n_\alpha \sigma_{A_i+\alpha_{\text{BG}} \rightarrow A_f+\dots}(E_{A_i}) \beta_{A_i} P_{A_f}, \quad (3.9)$$

where  $f_{A_i}$  is the energy distribution of  $A_i$  produced by the scattering or hadrodissociation processes of  $\alpha_{\text{BG}}$ ,  $(dE_{A_i}/dt)^{-1}$  is the energy-loss rate,  $\sigma_{A_i+\alpha_{\text{BG}} \rightarrow A_f+\dots}$  is the production cross section of  $A_f$ ,  $\beta_{A_i}$  is the velocity, and  $P_{A_f}$  is the survival probability of  $A_f$  after production. (For  $A_f = {}^6\text{Li}$ ,  $A_i = \text{T}$ ,  ${}^3\text{He}$ , and  ${}^4\text{He}$  contributes, while only  $A_i = {}^4\text{He}$  is relevant for  $A_f = {}^7\text{Li}$  and  ${}^7\text{Be}$ .) Then, for  $A_i = {}^6\text{Li}$ ,  ${}^7\text{Li}$  and  ${}^7\text{Be}$ , the Boltzmann equations are given in the following form:

$$\frac{dn_{A_i}}{dt} = \left[ \frac{dn_{A_i}}{dt} \right]_{\text{SBBN}} + \left[ \frac{dn_{A_i}}{dt} \right]_{\text{photodis}} + \left[ \frac{dn_{A_i}}{dt} \right]_{\gamma+\alpha_{\text{BG}} \rightarrow \dots} + n_X \Gamma_X \xi_{A_i}. \quad (3.10)$$

Here,  $[dn_{A_i}/dt]_{\gamma+\alpha_{\text{BG}} \rightarrow \dots}$  denotes the effects of the non-thermal production processes initiated by the photodissociation of  $\alpha_{\text{BG}}$  [16], which exists only for  $A_i = {}^6\text{Li}$ .

The expansion of the universe is determined by the Einstein equation; the expansion rate of the universe is calculated with taking into account the energy density of  $X$ . In addition, the effect of the entropy production due to the decay of  $X$  is included. Thus, the value of  $\eta$  is defined as the value after the entropy production.<sup>#8</sup> The initial value of the baryon number density is set to realize the required value of  $\eta$ . These effects are relevant for the parameter region in which  $X$  once dominates the universe. (As we will see below, however, such a parameter region is mostly excluded by the CMB constraints.)

## 4 Constraints on Generic Decaying Particles

### 4.1 Constraints from each light elements

We first investigate the BBN constraints on generic decaying particles. In Fig. 11 we show the constraints on the decaying particles which primarily decay into  $e^+e^-$  or  $b\bar{b}$ . In the figure, we show the constraints on the combination  $m_X Y_X$  (with  $m_X$  being the mass of  $X$ ) as functions of the lifetime  $\tau_X$  for the final states  $e^+e^-$  or  $b\bar{b}$ .<sup>#9</sup>

When the decaying particles mainly decay into  $e^+e^-$ , the hadronic branching ratio is small. In fact, hadrons are produced through the decay process  $X \rightarrow e^+ + e^- + q + \bar{q}$ , but the branching ratio for a such process is suppressed by  $\sim \mathcal{O}((\alpha/4\pi)^2) \sim 10^{-6}$ . Thus, most of the constraints are due to radiative decay. At the cosmic time  $\tau_X \sim 10^4 - 10^6$  sec, only D

<sup>#8</sup>We consider the case where the same amount of baryon and anti-baryon are produced in average by the decay. For the case of an asymmetric decay, see, for example, Ref. [49].

<sup>#9</sup>In the figures, in order to indicate the final state, we use the notation  $M_{FF'}$ , which is equal to  $m_X$ , where  $FF'$  corresponds to the final state particles of the  $X$  decay.

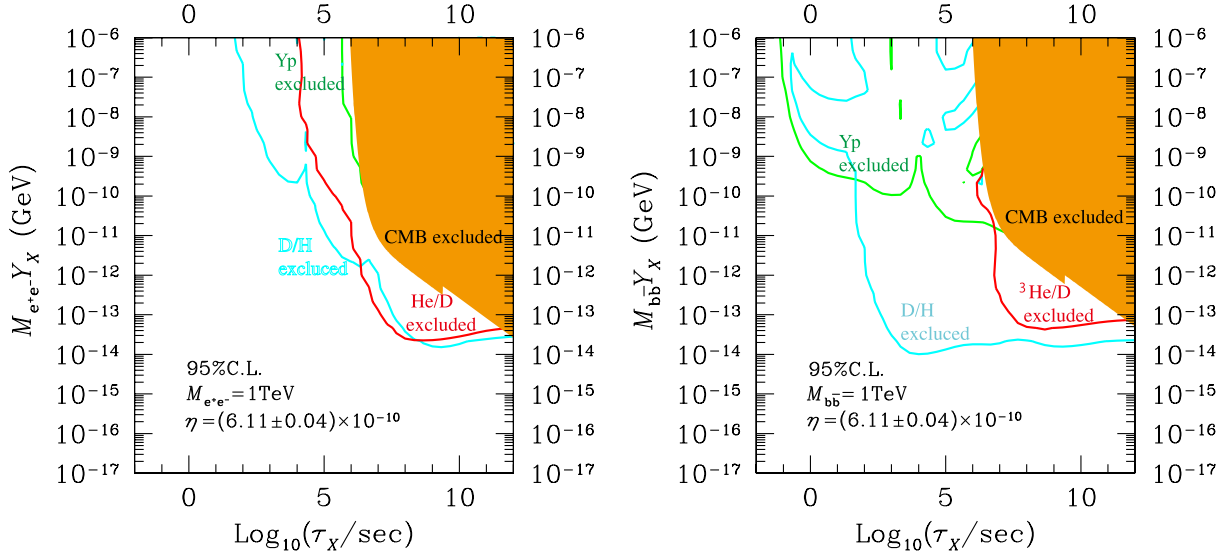


Figure 11: Constraints on  $m_X Y_X$  vs.  $\tau_X$  plane, assuming that the main decay modes are  $e^+e^-$  (left) or  $b\bar{b}$  (right) in case that the invariant mass into the daughter particles is  $m_X = 1\text{TeV}$ . The BBN constraints comes from  $^4\text{He}$  (green), D (cyan) and  $^3\text{He}/D$  (red). The orange shaded region is excluded by the CMB spectral distortion.

is destroyed by energetic photons that are not thermalized by photon-photon processes, so photodissociation of D gives the stringent constraint for  $\tau_X \sim 10^4 - 10^6$  sec. At  $t \gtrsim 10^6$  sec,  $^4\text{He}$  is also destroyed by photodissociation processes, which leads to non-thermal production of D and  $^3\text{He}$ . Thus, the stringent constraints are imposed by overproduction of D and  $^3\text{He}$ .<sup>#10</sup> It is seen that the abundance of the  $X$  is also constrained for  $\tau_X \lesssim 10^4$  sec, which is due to hadrodissociation of  $^4\text{He}$ . Since the photons with energy larger than  $\mathcal{O}(1)$  MeV are quickly thermalized at  $t \lesssim 10^4$  sec, they cannot destroy the light elements. On the other hand, hadrons like proton and neutron can destroy  $^4\text{He}$  and produce D and  $^3\text{He}$  non-thermally. The resultant constraint due to hadrons is weak because the hadronic branching ratio is small in this case.

In the case where the  $X$  mainly decays into  $b\bar{b}$  (Fig. 11 (right)), the stringent constraints come from hadrodissociation of the light elements. The high energy quarks emitted in the decay induce hadronic showers in which  $^4\text{He}$  nuclei are destroyed by energetic nucleons. The hadrodissociation of  $^4\text{He}$  leads to overproduction of D, which gives a stringent constraint, in particular, for  $\tau_X \sim 10^2 - 10^7$  sec. The photodissociation of  $^4\text{He}$  also produces D and gives a stringent constraint for  $\tau_X \gtrsim 10^7$  sec where effects of hadrodissociation and photodissociations are roughly comparable. In addition, non-thermal production of  $^3\text{He}$  by photodissociation gives a significant constraint for  $\tau_X \gtrsim 10^7$  sec. For  $\tau_X \lesssim 100$  sec the constraint coming

<sup>#10</sup>Notice that the present constraints from  $^3\text{He}/D$  and  $D/H$  are almost the same while in the previous work [28] the constraint from  $^3\text{He}/D$  was severer than that from  $D/H$ . This is because of the recent precise measurement of the abundance of  $D/H$ .

from  ${}^4\text{He}$  overproduction is most stringent. At the early stage of BBN ( $t \sim 1 - 100$  sec) interconversion of protons and neutrons is the most important process which almost determines the final  ${}^4\text{He}$  abundance. The strongly interacting conversion increases  $n/p$  from its standard value. As a result more  ${}^4\text{He}$  is produced, from which we obtain the constraint for  $\tau_X \lesssim 100$  sec. From the figure one notice that there appears the constraint from D/H for  $\tau_X \sim 0.1 - 100$  sec. The constraint around  $m_X Y_X \sim 10^{-9}$  GeV comes from overproduction of D due to larger  $n/p$ . Since the change of  $n/p$  affects the abundance of  ${}^4\text{He}$  more significantly, the D/H constraint is weaker. The D/H constraint around  $m_X Y_X \sim 10^{-7}$  GeV needs some caution. In this parameter region large  $n/p$  already makes the abundance of  ${}^4\text{He}$  much larger than the standard value. The D abundance is sensitive to the change of  ${}^4\text{He}$  abundance because D is residual after synthesizing  ${}^4\text{He}$ . The  ${}^4\text{He}$  abundance has  $\mathcal{O}(10)\%$  theoretical uncertainty in this parameter region, which drastically increases the uncertainty of the D abundance. As a result, it makes difficult to obtain a reliable constraint from D. Since this region is ruled out by overproduction of  ${}^4\text{He}$ , this is not an obstacle to obtain constraints on the properties of  $X$ .

In Fig. 11, the constraints from the CMB are also shown. When the decay of  $X$  injects electromagnetic energy into the background plasma, the spectrum of the CMB is distorted. Since photon number changing processes, like the double Compton scattering, are not efficient at  $t \gtrsim 10^7$  sec, the resultant CMB spectrum deviates from the Planck distribution if  $X$  decays at such an epoch [50, 51, 52]. The COBE set a stringent constraint on the spectrum distortion of the CMB [53], from which we obtain the upper bound on the abundance of  $X$ , as shown in Fig 11. It is seen that the BBN constraints are more stringent than those from the CMB for both decay modes.<sup>#11</sup> Notice that future observations of the CMB spectrum such as PIXIE will improve the bounds by a factor of 100 – 500 [54].

## 4.2 Constraints on various decay modes

Now, we show constraints for the cases with various main decay modes.

We first consider the cases where  $X$  decays into colored particles. In Fig. 12 we show the combined constraints on the abundance and lifetime of  $X$  whose main decay mode is  $u\bar{u}$ ,  $b\bar{b}$ ,  $t\bar{t}$  or  $gg$ ; in Fig. 12, only the most stringent constraint is shown combining the constraints from D,  ${}^4\text{He}$ , and  ${}^3\text{He}/\text{D}$ . For all the decay modes shown in this figure, the decay products are colored particles and produce hadronic showers whose total energy is roughly equal to  $m_X$ . Therefore, the resultant constraints are similar. As described above, hadrons produced by the decay affects the BBN for  $\tau_X \lesssim 10^7$  sec. As a result, the constraints from overproduction of  ${}^4\text{He}$  due to the enhancement of  $n/p$  is most stringent for  $\tau_X \lesssim 10^2$  sec while overproduction of D via hadrodissociation of  ${}^4\text{He}$  gives the strongest constraint for  $\tau_X \gtrsim 10^2 - 10^7$  sec. We also show how the constraints depend on  $m_X$ , taking  $m_X = 0.03, 0.1, 1, 10, 100$  and  $1000$  TeV. Since the number of hadrons produced through the hadronization process depends on  $m_X$  as  $m_X^\delta$  with  $\delta \sim 0.3$ , the constraints on  $m_X Y_X$  from hadrodissociation become weaker as  $m_X$  increases. On the other hand, the most stringent constraints for  $\tau_X \gtrsim 10^7$  sec come

<sup>#11</sup> See also Ref. [55], for a possible mass dependence on this relation.

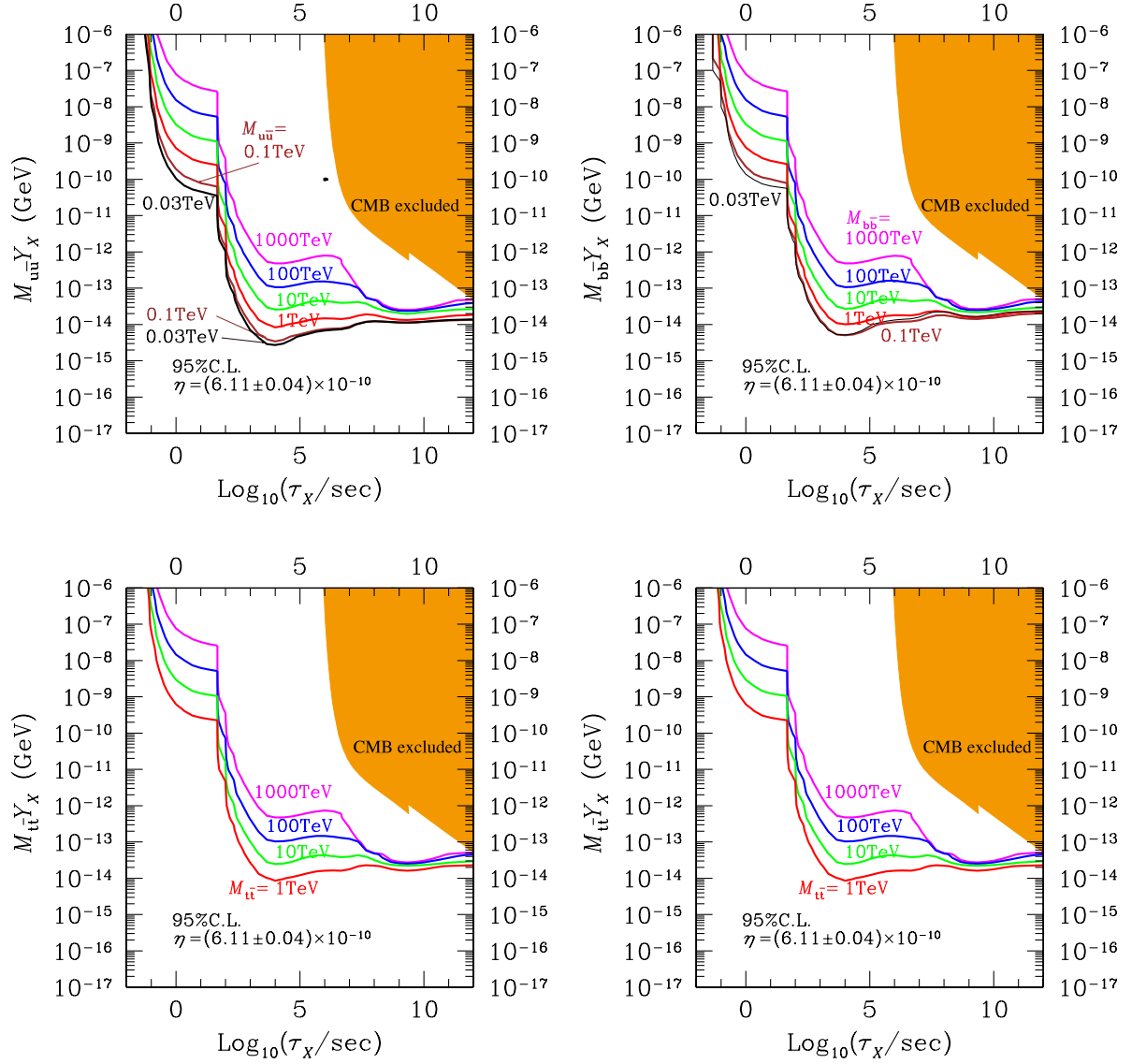


Figure 12: Constraints on  $m_X Y_X$  vs.  $\tau_X$  plane, assuming that the main decay modes are  $u\bar{u}$  (upper left),  $b\bar{b}$  (upper right),  $t\bar{t}$  (lower left) and  $g g$  (lower right). The black, dark-red, red, green, blue and magenta solid lines denote the BBN constraints for  $m_X = 0.03, 0.1, 1, 10, 100$  and  $1000 \text{ TeV}$ , respectively. The orange shaded regions are excluded by the constraint from the CMB spectral distortion.

from the photodissociation of  ${}^4\text{He}$ , which leads to the overproduction of D and  ${}^3\text{He}$ . Since the effects of photodissociations are determined by the total energy injection, the constraint only depends on  $m_X Y_X$  as confirmed in Fig. 12.

In Fig. 13, we show the combined constraints on  $X$  which mainly decays into  $e^+e^-$ ,  $\tau^+\tau^-$ ,  $\gamma\gamma$  or  $W^+W^-$ , taking  $m_X = 0.03, 0.1, 1, 10, 100$  and  $1000$  TeV. For the decay into  $e^+e^-$ , as described in Section 4.1, the constraints are determined by the photodissociation effect for  $\tau_X \gtrsim 10^4$  sec (destruction of D for  $\tau_X \sim 10^4 - 10^6$  sec and overproduction of  ${}^3\text{He}$  for  $\tau_X \gtrsim 10^6$  sec). Because the branching ratio into  $q\bar{q}$  is small, the effect of hadronic decay is significant only for  $\tau_X \lesssim 10^4$  sec where photodissociation does not take place. The constraints for the case that  $X$  mainly decays into  $\tau^+\tau^-$  is also shown. Since the branching ratio into  $q\bar{q}$  is as small as the  $e^+e^-$  case, the constraints for  $\tau_X \gtrsim 10^4$  sec are almost same as Fig. 13 (upper left); the constraints are slightly weaker because some amount of the energy is carried away by neutrinos. The effect of hadrodissociation is seen for  $\tau_X \lesssim 10^4$  sec, which is similar to the  $e^+e^-$  decay. The constraints from the change of  $n/p$  are seen for  $\tau_X \lesssim 10^2$  sec, which is due to the mesons produced by the  $\tau$  decay. The constraints on the decay mode  $\gamma\gamma$  are shown in Fig. 13 (lower left). For  $\tau_X \gtrsim 10^6$  sec, photodissociation is important and the constraint is similar to that for  $e^+e^-$  decay. However, compared to the  $e^+e^-$  case, the  $q\bar{q}$  production rate at the decay is relatively large,  $\sim \mathcal{O}(\alpha/4\pi) \sim 10^{-4} - 10^{-3}$ . Therefore, the constraints from the hadronic processes is more important than that from photodissociation for  $\tau_X \lesssim 10^6$  sec. In Fig. 13 (lower right), we show the constraints on the decay into  $W^+W^-$ . Since  $W$  bosons further decay into hadrons with branching ratio of about 0.67, effects of the hadronic decay are important and hence the resultant constraints looks similar to those on  $q\bar{q}$  decay modes.

So far we have adopted Eq. (2.4) as the observational constraint of  ${}^4\text{He}$ . Now let us see how the constraints change if we adopt the other constraint (2.3). In Fig. 14, the BBN constraints from D,  ${}^3\text{He}/\text{D}$  and  ${}^4\text{He}$  are shown, assuming that the main decay mode is  $b\bar{b}$ . As mentioned in Section 2, the  ${}^4\text{He}$  abundance (2.3) estimated by Izotov, Thuan and Guseva is significantly larger than that obtained by Aver, Olive and Skillman given in Eq. (2.4) and not consistent with SBBN if we use the baryon-to-photon ratio determined by Planck. Their observation becomes consistent with BBN if the abundance of  ${}^4\text{He}$  is increased by the decay of  $X$ . When  $X$  mainly decays into  $b\bar{b}$ , there appears a region consistent with Eq. (2.3) as well as with other light element abundances, i.e.,  $\tau_X \sim 10^{-1} - 10^4$  sec and  $m_X Y_X \sim 10^{-10} - 10^{-6}$  GeV. This is due to the effect that the decay of  $X$  with such lifetime induces the  $p \leftrightarrow n$  conversion, resulting in the increase of the abundance of  ${}^4\text{He}$ . If the  ${}^4\text{He}$  abundance (2.3) is confirmed, it may suggest the existence of a long-lived hadronically decaying particle which solves the discrepancy between SBBN and Eq. (2.3). On the other hand, if the hadronic branching ratio is much smaller, like the case that the main decay mode is  $e^+e^-$ , there is no region consistent with Eq. (2.3) together with observational constraints on D and  ${}^3\text{He}/\text{D}$ .

Before closing this section, we comment on the effects of the decaying particles on abundances of  ${}^7\text{Li}$  and  ${}^6\text{Li}$  although we do not use them to derive the constraints on the decaying particles. In Fig. 15, abundances of  ${}^7\text{Li}$  and  ${}^6\text{Li}$  are shown, assuming that the main decay mode is  $b\bar{b}$  or  $e^+e^-$ . Notably, for  $\tau_X \sim 10^2 - 10^3$  sec, primordial  ${}^7\text{Li}$  abundance is reduced by

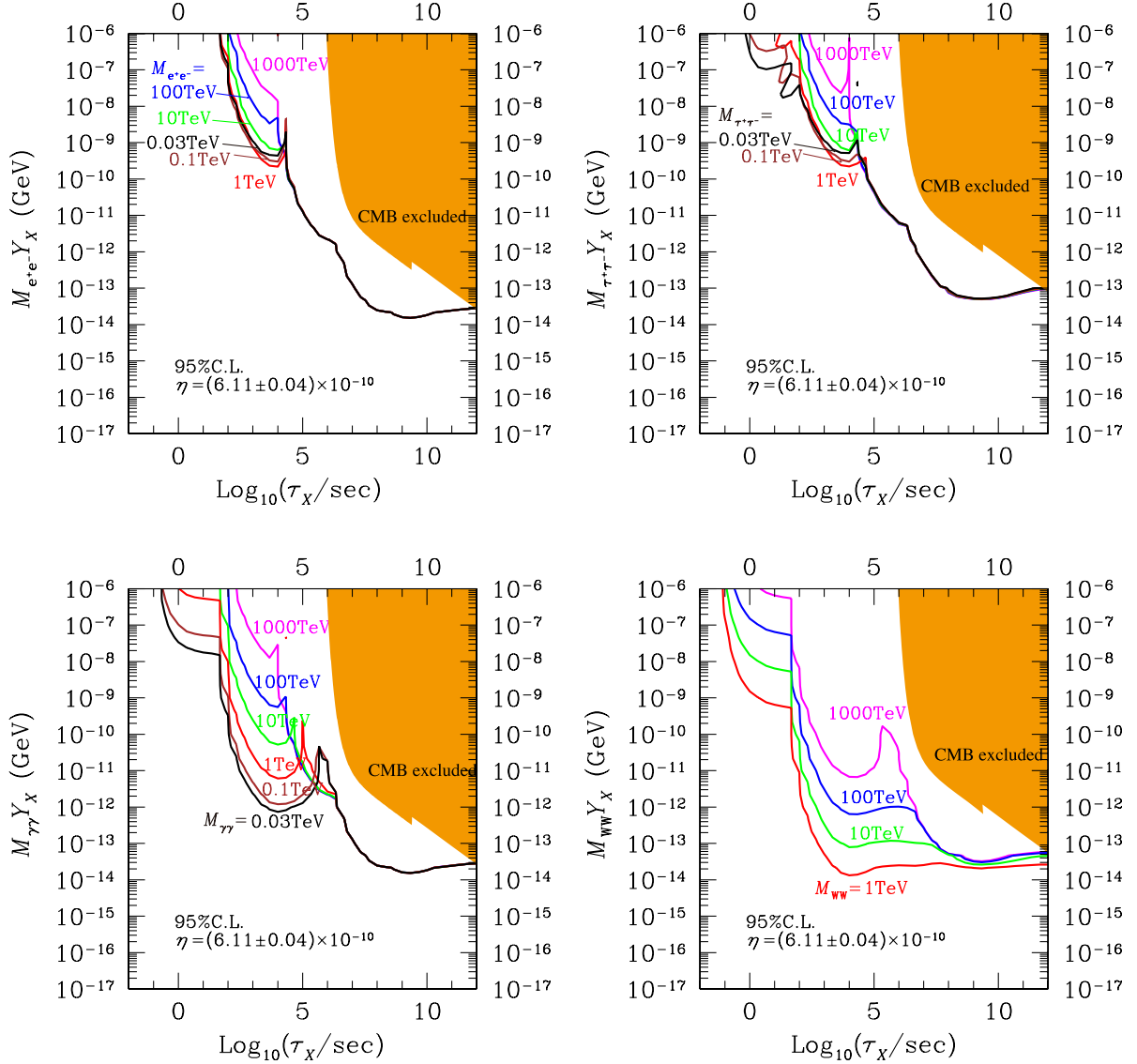


Figure 13: Constraints on  $m_X Y_X$  vs.  $\tau_X$  plane, assuming that the main decay modes are  $e^+e^-$  (upper left),  $\tau^+\tau^-$  (upper right),  $\gamma\gamma$  (lower left) and  $W^+W^-$  (lower right). The black, dark-red, red, green, blue and magenta solid lines denote the BBN constraints for  $m_X = 0.03, 0.1, 1, 10, 100$  and  $1000$  TeV, respectively. The orange shaded regions are excluded by the constraint from the CMB spectral distortion.

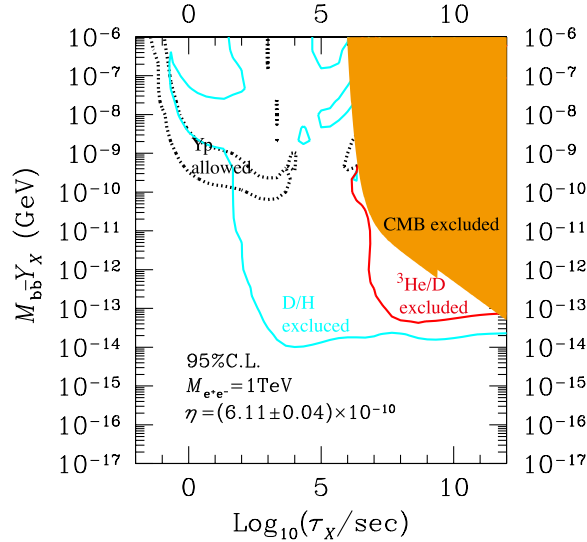


Figure 14: Constraints on  $m_X Y_X$  vs.  $\tau_X$  plane, assuming that  $m_X = 1$  TeV and that the main decay mode is  $b\bar{b}$ . The solid cyan, solid red and dashed lines denote the BBN constraints from D,  ${}^3\text{He}/\text{D}$  and  ${}^4\text{He}$ , respectively. Here, we use Eq. (2.3) as the observational constraint on  $Y_p$ . The orange shaded region is excluded by the CMB spectral distortion.

non-thermal neutrons;  ${}^7\text{Be}$ , which is one of the origins of primordial  ${}^7\text{Li}$ , can be converted to  ${}^7\text{Li}$  by non-thermal neutrons as  ${}^7\text{Be} + n \rightarrow {}^7\text{Li} + p$ , then  ${}^7\text{Li}$  is destroyed by the SBBN reaction  ${}^7\text{Li} + p \rightarrow {}^4\text{He} + {}^4\text{He}$ . Such effects may dominate over the non-thermal production of  ${}^7\text{Li}$  due to energetic T,  ${}^3\text{He}$ , and  ${}^4\text{He}$  from the photodissociation and scattering of  ${}^4\text{He}$ , resulting in the net decrease of the  ${}^7\text{Li}$  abundance. For the case of  $b\bar{b}$  mode, the constraints from D/H,  ${}^3\text{He}/\text{D}$  and  ${}^4\text{He}$  exclude the parameter region where the  ${}^7\text{Li}$  abundance significantly decreases. On the other hand,  ${}^7\text{Li}$  abundance can be reduced for the main decay mode of  $e^+e^-$  without conflicting with other constraints, if  $\tau_X \sim \mathcal{O}(100)$  sec and  $m_X Y_X \sim 10^{-7}$  GeV. This might provide a solution to the  ${}^7\text{Li}$  problem in SBBN.

In Fig. 15 it is seen that non-thermal production of  ${}^6\text{Li}$  due to the decaying particles is significant for  $\tau_X \gtrsim 10^3$  sec. Taking into account the constraints from the other light elements,  ${}^6\text{Li}/{}^7\text{Li}$  can be as large as  $10^{-2}$  for the  $b\bar{b}$  decay mode, while it can be  $\mathcal{O}(0.1)$  for the  $e^+e^-$  mode. On the contrary,  ${}^6\text{Li}$  is hardly produced in SBBN (i.e.,  ${}^6\text{Li}/{}^7\text{Li} \lesssim 10^{-4}$ ). Thus, if a significant amount of  ${}^6\text{Li}/{}^7\text{Li}$  is observed in low-metal stars, it would give an evidence for the existence of decaying particles in the early universe. In particular, for the  $e^+e^-$  mode, it is remarkable that  ${}^6\text{Li}/{}^7\text{Li}$  is significantly large with simultaneously solving the  ${}^7\text{Li}$  problem at around  $\tau_X \sim 10^3$  sec and  $m_X Y_X \sim 10^{-7.5}$  GeV.

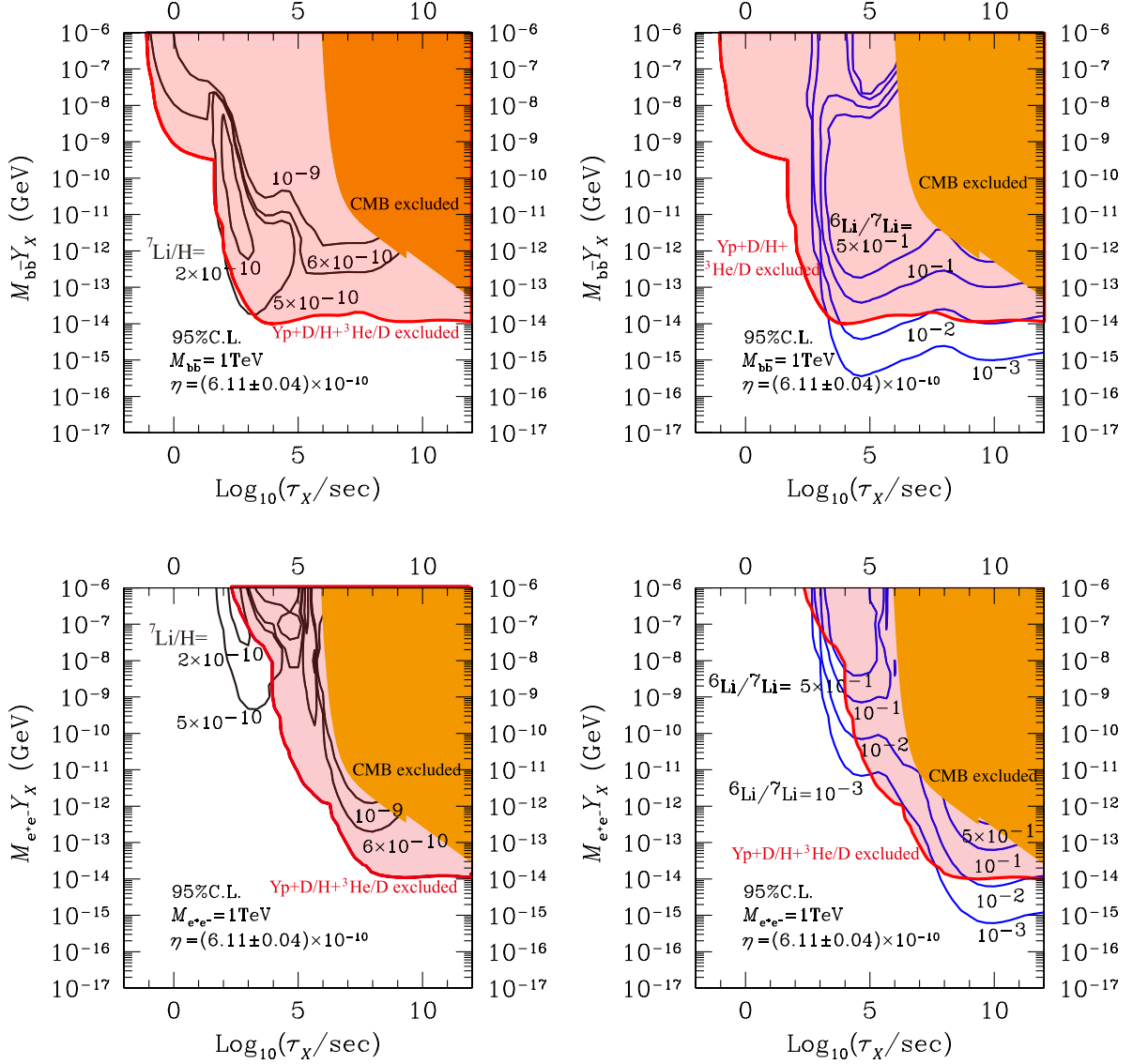


Figure 15: Abundances of  ${}^7\text{Li}/\text{H}$  (left) and  ${}^6\text{Li}/{}^7\text{Li}$  (right) for decay particles with mass 1 TeV which decay mainly into  $\bar{b}b$  (upper) and  $e^+e^-$  (lower). The constraints from other light elements and CMB are shown in pink shaded region (surrounded by red solid line) and orange shaded region, respectively.

## 5 Gravitino

One of the important candidates of long-lived particles is gravitino in SUSY models. Gravitino is the superpartner of graviton, and interacts very weakly because its interaction is suppressed by inverse powers of the (reduced) Planck scale  $M_{\text{Pl}} \simeq 2.4 \times 10^{18}$  GeV. Because of the weakness of its interaction, the lifetime of gravitino may become so long that its decay products affect the light element abundances (if gravitino is unstable). Assuming  $R$ -parity conservation, gravitino becomes unstable if it is not the lightest superparticle (LSP). Even when gravitino is the LSP, the next-to-the lightest superparticle (NLSP) decays into gravitino with very long lifetime, and hence the BBN constraints on the properties of the NLSP are derived, e.g., see Refs. [31, 56]. Here, we pay particular attention to the former case where gravitino is unstable because, in such a case, we can obtain an upper bound on the reheating temperature after inflation in order not to overproduce gravitino. Applying the analysis of the non-standard BBN processes discussed in the previous sections, we study the effects of the gravitino decay on the light element abundances and derive the upper bound on the reheating temperature.

The primordial abundance of gravitino is sensitive to the reheating temperature after inflation,<sup>#12</sup> which we define

$$T_{\text{R}} \equiv \left( \frac{10}{g_*(T_{\text{R}})\pi^2} M_{\text{Pl}}^2 \Gamma_{\text{inf}}^2 \right)^{1/4}, \quad (5.1)$$

with  $\Gamma_{\text{inf}}$  being the decay rate of the inflaton, and  $g_*(T_{\text{R}})$  being the effective number of the massless degrees of freedom at the time of reheating. In our study, we use the value suggested by the minimal SUSY standard model (MSSM),  $g_*(T_{\text{R}}) = 228.75$ .

Gravitino is produced via the scattering processes of MSSM particles in the thermal bath. The Boltzmann equation for the number density of gravitino (denoted as  $n_{3/2}$ ) is given by

$$\frac{dn_{3/2}}{dt} + 3Hn_{3/2} = C_{3/2}, \quad (5.2)$$

where  $C_{3/2}$  is the thermally averaged collision term. The most precise calculation of the collision term includes hard thermal loop resummation to avoid infrared singularity [60, 61, 62], and  $C_{3/2}$  is parametrized as

$$C_{3/2} = \sum_{i=1}^3 \frac{3\zeta(3)T^6}{16\pi^3 M_{\text{Pl}}^2} \left( 1 + \frac{M_i^2(T)}{3m_{3/2}^2} \right) c_i g_i^2 \ln \left( \frac{k_i}{g_i} \right), \quad (5.3)$$

where  $i = 1, 2$ , and  $3$  correspond to the gauge groups  $U(1)_Y$ ,  $SU(2)_L$ , and  $SU(3)_C$ , respectively. Here,  $M_i(T)$  are the gaugino mass parameters at the renormalization scale  $Q = T$ , and  $g_i$  are the gauge coupling constants. In addition,  $c_i$  and  $k_i$  are numerical

---

<sup>#12</sup>Gravitino may be also produced non-thermally by the decay of the moduli fields or inflaton field [57, 58, 59]. We do not consider such contributions in our study to derive a conservative bound on the reheating temperature after inflation.

constants. Refs. [60, 61] give  $(c_1, c_2, c_3) = (11, 27, 72)$  and  $(k_1, k_2, k_3) = (1.266, 1.312, 1.271)$ , while the coefficients from Ref. [62] are  $(c_1, c_2, c_3) = (9.90, 20.77, 43.34)$  and  $(k_1, k_2, k_3) = (1.469, 2.071, 3.041)$ .<sup>#13</sup>

As one can see, the collision term is typically  $C_{3/2} \sim T^6/M_{\text{Pl}}^2$  (as far as  $T$  is higher than the masses of MSSM particles). Then, the yield variable of gravitino, which is defined as  $Y_{3/2}$  hereafter, is approximately proportional to the reheating temperature for the parameter region of our interest. Consequently, the BBN constraints on the gravitino abundance can be converted to the upper bound on the reheating temperature  $T_{\text{R}}$ .

We numerically solve the Boltzmann equation (5.2) (as well as the evolution equation of the universe based on Einstein equation) to accurately calculate the primordial abundance of gravitino. Assuming the MSSM particle content up to the GUT scale, the gravitino abundance can be well fit by the following formula:

$$Y_{3/2} \simeq y_0 T_{\text{R}}^{(8)} \left[ 1 + \delta_0^{(1)} \ln T_{\text{R}}^{(8)} + \delta_0^{(2)} \ln^2 T_{\text{R}}^{(8)} \right] + \sum_{i=1}^3 y_i T_{\text{R}}^{(8)} \left[ 1 + \delta_i^{(1)} \ln T_{\text{R}}^{(8)} + \delta_i^{(2)} \ln^2 T_{\text{R}}^{(8)} \right] \left( \frac{M_i^{(\text{GUT})}}{m_{3/2}} \right)^2, \quad (5.4)$$

where  $T_{\text{R}}^{(8)} \equiv T_{\text{R}}/10^8$  GeV and  $M_i^{(\text{GUT})}$  are the gaugino masses at the GUT scale which is taken to be  $2 \times 10^{16}$  GeV in our analysis. Numerical constants in the above fitting formula based on Refs. [60, 61] and those for Ref. [62] are summarized in Tables 1 and 2, respectively. The primordial abundance of gravitino based on Refs. [60, 61] is smaller than that based on Ref. [62]. Thus, we perform our numerical analysis with the former set of the coefficients in order to derive a conservative constraint. The bound based on Ref. [62] can be obtained by translating the bound on  $T_{\text{R}}$  to that on the primordial abundance  $Y_{3/2}$  using, for e.g., Eq. (5.4); the bound on  $T_{\text{R}}$  based on Ref. [62] is at most 2 – 3 times more stringent than that based on Refs. [60, 61].

Because the interaction of gravitino is governed by the SUSY, the partial decay rates of gravitino are determined once the mass spectrum of the MSSM particles are known. For a precise calculation of the upper bound on the reheating temperature, we fix the mass spectrum of the MSSM particles and calculate the decay widths of gravitino. We consider several sample points; the mass spectrum of each sample point is summarized in Table 3. The sample point 1 is based on so-called CMSSM [64] parametrized by the universal scalar mass  $m_0$ , unified gaugino mass  $M_{1/2}$ , universal tri-linear coupling constants  $A_0$  (with respect to the corresponding Yukawa coupling constants),  $\tan \beta$  (which is the ratio of the vacuum expectation values of up- and down-type Higgs bosons), and the sign of the SUSY invariant Higgs mass parameter  $\mu$ . For the sample point 1, we take  $m_0 = 433$  GeV,  $M_{1/2} = 970$  GeV,  $A_0 = -3020$  GeV,  $\tan \beta = 14$ , and  $\mu > 0$ . As one can see, in the sample point 1, all the MSSM particles are lighter than  $\sim 2.5$  TeV, and the discovery of some of the MSSM particles are expected in future LHC experiment. The sample point 2 is also based on the CMSSM, with the underlying parameters of  $m_0 = 5000$  GeV,  $M_{1/2} = 700$  GeV,  $A_0 = -8000$  GeV,

<sup>#13</sup>For the latter, we use the coefficients given in Ref. [63], which is based on Ref. [62].

	$i = 0$	$i = 1$	$i = 2$	$i = 3$
$y_i$	$2.3 \times 10^{-14}$	$1.3 \times 10^{-16}$	$1.6 \times 10^{-15}$	$1.3 \times 10^{-14}$
$\delta_i^{(1)}$	0.015	0.055	0.013	-0.042
$\delta_i^{(2)}$	-0.0005	0.0081	0.0001	0.0006

Table 1: Numerical constants for the formula (5.4), which gives a fitting formula for the primordial gravitino abundance, based on Refs. [60, 61].

	$i = 0$	$i = 1$	$i = 2$	$i = 3$
$y_i$	$4.4 \times 10^{-14}$	$1.5 \times 10^{-16}$	$2.1 \times 10^{-15}$	$3.2 \times 10^{-14}$
$\delta_i^{(1)}$	-0.014	0.066	0.015	-0.089
$\delta_i^{(2)}$	0.0054	0.0042	0.0002	0.0031

Table 2: Numerical constants for the formula (5.4) based on Ref. [62].

$\tan \beta = 10$  and  $\mu > 0$ . At this point, the  $\mu$ -parameter is relatively small, and the Higgsino-like neutralino becomes the LSP. In the sample points 3 and 4, we consider the case where the sfermion masses are above 100 TeV while gaugino masses are around the TeV scale.<sup>#14</sup> Such a mass spectrum is motivated in the so-called pure gravity mediation model [65, 66, 67], in which scalar masses originate from a direct Kähler interaction between the SUSY breaking field and the MSSM chiral multiplet, while the gaugino masses are from the effect of anomaly mediation [68, 69]. Then, the gaugino masses are given in the following form:

$$M_1 = \frac{g_1^2}{16\pi^2} (11F_\Phi + L), \quad (5.5)$$

$$M_2 = \frac{g_2^2}{16\pi^2} (F_\Phi + L), \quad (5.6)$$

$$M_3 = \frac{g_3^2}{16\pi^2} (-3F_\Phi), \quad (5.7)$$

where  $F_\Phi$  is the expectation value of the compensator multiplet,<sup>#15</sup> while  $L$  parametrizes the effect of Higgs-Higgsino loop on the gaugino masses. In a large class of models,  $L$  is of order  $F_\Phi$  for the scale below the masses of heavy Higgses and Higgsinos. The gaugino masses for the sample points 3 and 4 are obtained by adopting  $(F_\Phi, L) = (131 \text{ TeV}, 218 \text{ TeV})$ , and  $(82 \text{ TeV}, 87 \text{ TeV})$ , respectively. Notice that, above the mass scale of the heavy Higgs

<sup>#14</sup>Eq. (5.4) is applicable only when the mass scale of the MSSM particles is lower than the reheating temperature. Although this condition is not satisfied when  $T_R \lesssim 10^5 \text{ GeV}$  for sample points 3 and 4, we use Eq. (5.4) throughout our analysis. As we will see below, the upper bound on  $T_R$  is found to be at least  $\sim 10^5 \text{ GeV}$ , and our approximation is marginally acceptable for the reheating temperature of our interest.

<sup>#15</sup>In the model where the vacuum expectation value of the SUSY breaking field is much smaller than the Planck scale,  $F_\Phi = m_{3/2}$ . In this analysis, however, we consider more general framework, and treat  $F_\Phi$  as a free parameter.

and Higgsino, the gaugino mass parameters are obtained by Eqs. (5.5) – (5.7), with taking  $L \rightarrow 0$ . For the calculation of the primordial abundance of gravitino, we take account of this effect, and the thermally averaged gravitino production cross sections for the points 3 and 4 are evaluated by taking vanishing  $L$ .

With fixed mass spectrum of the MSSM particles, we vary the gravitino mass and derive the upper bound on the reheating temperature as a function of the gravitino mass. In our calculation, all the two-body tree-level decay processes of gravitino are taken into account. We also include three-body decay processes  $\tilde{G} \rightarrow \tilde{\chi}_0 q \bar{q}$  (with  $\tilde{G}$ ,  $\tilde{\chi}_0$  and  $q$  denoting gravitino, the lightest neutralino and  $u$ ,  $d$ ,  $s$ ,  $c$  or  $b$  quark, respectively), if the mass splitting between gravitino and the lightest neutralino is less than the  $Z$ -boson mass. This is because those three-body decay processes can have substantial contribution to hadronic emissions from gravitino decays to the lightest neutralino when the two-body decay process  $\tilde{G} \rightarrow \tilde{\chi}_1^0 Z$  is kinematically forbidden. For the sample points 3 and 4, the lightest chargino ( $\tilde{\chi}_1^\pm$ ) has degenerate mass with the lightest neutralino and behaves as the LSP. We therefore include the off-shell  $W^\pm$  induced three-body decay processes,  $\tilde{G} \rightarrow \tilde{\chi}_1^\pm q \bar{q}'$ , as well in our calculation if  $m_{3/2} - m_{\tilde{\chi}_1^\pm} < m_W$ .

The partial decay rates of gravitino are calculated by using MadGraph5\_aMC@NLO v2.1 package [70] with gravitino interactions being implemented via FeynRules v2.3 [71, 72, 73, 74]. Subsequent decay and the hadronization processes of the decay products of gravitino are simulated by using PYTHIA 8.2 package [42]. For given reheating temperature, the primordial abundance of gravitino is calculated by numerically solving Eq. (5.2). For the thermally averaged gravitino production cross section, we adopt the results of Refs. [60, 61].

Following the procedure discussed in the previous sections, we calculate the light element abundances, taking into account the effects of the decay products of gravitino. The constraints on the gravitino abundance is then translated to the upper bound on the reheating temperature. The upper bound on  $T_R$  for the sample points 1, 2, 3, and 4 are shown in Fig. 16. As one can see, a severe upper bound of  $\sim 10^5 - 10^6$  GeV is obtained from the overproduction of D for relatively light gravitino mass (i.e., for  $m_{3/2} \lesssim$  a few TeV). This is because, when gravitino is lighter than a few TeV, the lifetime of gravitino is longer than  $\sim 10^3$  sec so that the constraint from D is significant, as discussed in the previous section. On the contrary, for heavier gravitino mass (i.e., for  $m_{3/2} \gtrsim 10$  TeV), for which the lifetime of gravitino becomes shorter than  $\sim 10^2$  sec, the most stringent constraint comes from the overproduction of  ${}^4\text{He}$  due to the  $p \leftrightarrow n$  conversion.

We also comment on the constraints based on the  ${}^4\text{He}$  abundance given in Eq. (2.3), which is inconsistent with the SBBN prediction. As mentioned in the previous section, with a hadronically decaying long-lived particle, the primordial  ${}^4\text{He}$  abundance may become consistent with Eq. (2.3). In the present case, gravitino has sizable branching ratio for hadronic decay modes. In Fig. 16, we also show a region consistent with the  ${}^4\text{He}$  abundance (2.3) estimated by Izotov, Thuan and Guseva. We can see that the allowed region exists for  $m_{3/2} \sim \mathcal{O}(10)$  TeV and  $T_R \sim \mathcal{O}(10^9)$  GeV.

Notice that the reheating temperature is bounded from above in order not to overclose the universe by the LSP produced from the decay of gravitino. For the parameter region of our interest, gravitino decays at the cosmic temperature lower than the freeze-out temperature

	Point 1	Point 2	Point 3	Point 4
$m_{\tilde{u}_{R,1,2}}$	1907	5242	$\sim 1 \times 10^5$	$\sim 1 \times 10^5$
$m_{\tilde{d}_{R,1,2}}$	1898	5054	$\sim 1 \times 10^5$	$\sim 1 \times 10^5$
$m_{\tilde{u}_{L,1,2}}(m_{\tilde{d}_{L,1,2}})$	1980 (1982)	5082 (5083)	$\sim 1 \times 10^5$	$\sim 1 \times 10^5$
$m_{\tilde{e}_{R,1,2}}$	562	4801	$\sim 1 \times 10^5$	$\sim 1 \times 10^5$
$m_{\tilde{e}_{L,1,2}}(m_{\tilde{\nu}_{L,1,2}})$	771 (767)	5093 (5092)	$\sim 1 \times 10^5$	$\sim 1 \times 10^5$
$m_{\tilde{t}_1}$	977	1455	$\sim 1 \times 10^5$	$\sim 1 \times 10^5$
$m_{\tilde{t}_2}$	1635	3603	$\sim 1 \times 10^5$	$\sim 1 \times 10^5$
$m_{\tilde{b}_1}$	1608	3607	$\sim 1 \times 10^5$	$\sim 1 \times 10^5$
$m_{\tilde{b}_2}$	1843	4990	$\sim 1 \times 10^5$	$\sim 1 \times 10^5$
$m_{\tilde{\tau}_1}$	417	4735	$\sim 1 \times 10^5$	$\sim 1 \times 10^5$
$m_{\tilde{\tau}_2}$	732	5062	$\sim 1 \times 10^5$	$\sim 1 \times 10^5$
$m_{\tilde{\nu}_{\tau L}}$	723	5061	$\sim 1 \times 10^5$	$\sim 1 \times 10^5$
$m_{\chi_1^0}$	417	187	1000	500
$m_{\chi_2^0}$	791	-209	1470	880
$m_{\chi_3^0}$	-1836	321	$\sim 1 \times 10^5$	$\sim 1 \times 10^5$
$m_{\chi_4^0}$	1838	618	$\sim 1 \times 10^5$	$\sim 1 \times 10^5$
$m_{\chi_1^\pm}$	791	199	1000	500
$m_{\chi_2^\pm}$	1839	618	$\sim 1 \times 10^5$	$\sim 1 \times 10^5$
$m_{\tilde{g}}$	2131	1817	3000	2000
$m_h$	124	126	125	125
$m_A$	1906	1000	$\sim 1 \times 10^5$	$\sim 1 \times 10^5$
$M_{1,2,3}^{(\text{GUT})}$	970	700	(2583, 376, -1137)	(1619, 236, -716)

Table 3: The mass spectrum of the MSSM particles as well as the gaugino masses at the GUT scale for the sample points adopted in our analysis. Here,  $m_{\tilde{u}_{R,i}}$  and  $m_{\tilde{u}_{L,i}}$  ( $m_{\tilde{d}_{R,i}}$  and  $m_{\tilde{d}_{L,i}}$ ) are masses of right- and left-handed sups (sdowns) in  $i$ -th generation, respectively, while  $m_{\tilde{e}_{R,i}}$  and  $m_{\tilde{e}_{L,i}}$  ( $m_{\tilde{\nu}_{L,i}}$ ) are masses of right- and left-handed charged sleptons (sneutrinos) in  $i$ -th generation, respectively. In addition,  $m_{\tilde{t}_1}$ ,  $m_{\tilde{b}_1}$ , and  $m_{\tilde{\tau}_1}$  ( $m_{\tilde{t}_2}$ ,  $m_{\tilde{b}_2}$ , and  $m_{\tilde{\tau}_2}$ ) are lighter (heavier) stop, sbottom, and stau masses, respectively, while  $m_{\tilde{\nu}_{\tau L}}$  is the tau-sneutrino mass. Furthermore,  $m_{\chi_i^0}$ ,  $m_{\chi_i^\pm}$ , and  $m_{\tilde{g}}$  are neutralino, chargino, and gluino masses, respectively, while  $m_h$  and  $m_A$  are masses of the lightest Higgs boson and CP-odd Higgs boson, respectively. All the mass parameters are given in units of GeV.

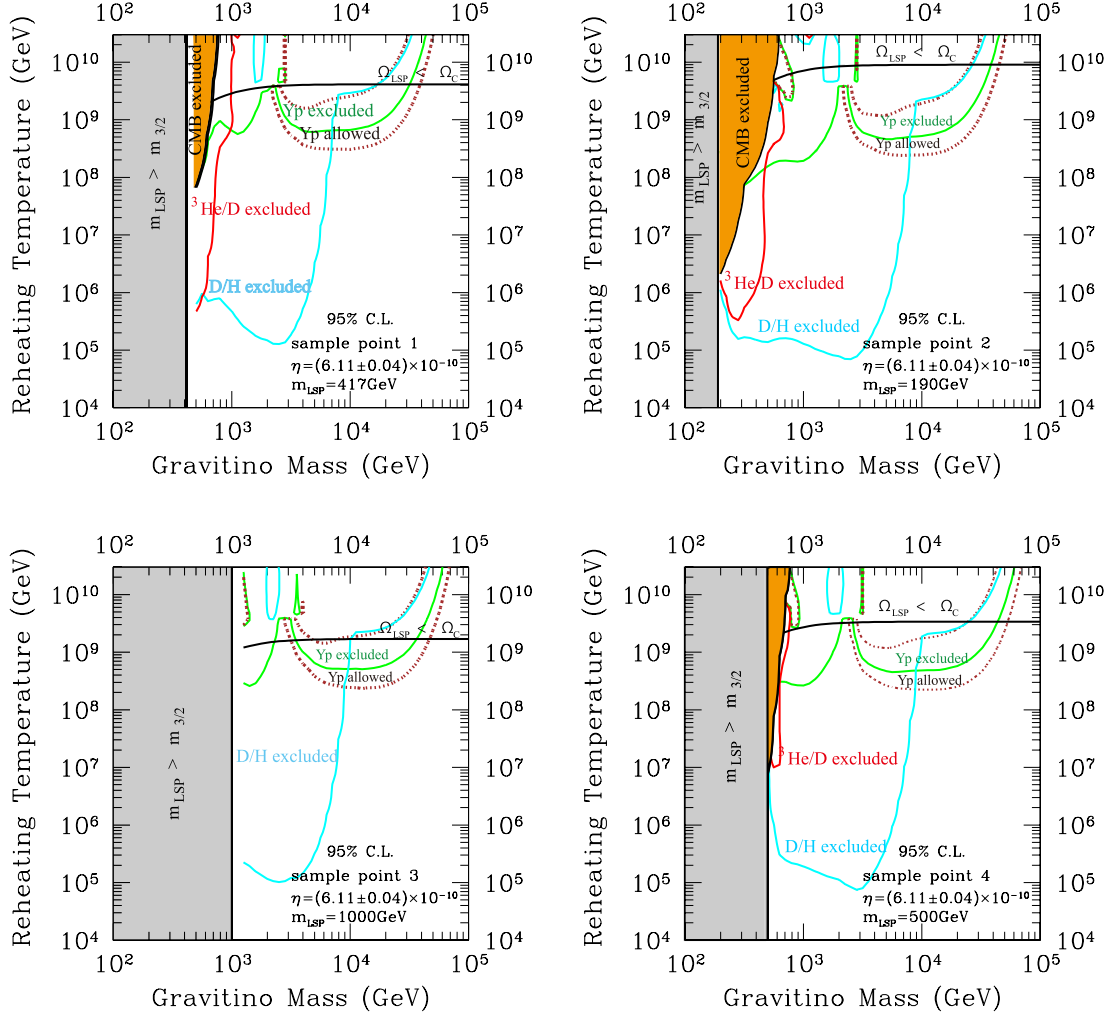


Figure 16: Upper bound on the reheating temperature  $T_R$  as a function of  $m_{3/2}$  at 95% C.L. for models of Point 1 (upper left), Point 2 (upper right), Point 3 (lower left), and Point 4 (lower right), respectively. The regions surrounded by the brown-dotted line indicate the region consistent with Eq. (2.3).

of the LSP. Thus, the density parameter of the LSP from the decay of gravitino is evaluated as

$$\Omega_{\text{LSP}}^{(\text{decay})} = \frac{m_{\text{LSP}} Y_{3/2} s_{\text{now}}}{\rho_{\text{crit}}}, \quad (5.8)$$

where  $s_{\text{now}}$  is the entropy density of the present universe, and  $\rho_{\text{crit}}$  is the critical density. We show the contour of  $\Omega_{\text{LSP}}^{(\text{decay})} = \Omega_c$  (with  $\Omega_c \simeq 0.26$  [41] being the density parameter of the cold dark matter).<sup>#16</sup> We can see that, with the present choice of the MSSM mass spectrum, the upper bound from the overclosure of the universe is  $10^9 - 10^{10}$  GeV, which is

<sup>#16</sup>If the thermal relic abundance of the LSP is sizable, the bound should be imposed on the total mass

less stringent when the gravitino mass is smaller than  $\sim 40 - 50$  TeV.

Before closing this section, we comment on the implication of our result on the leptogenesis [75], in which the baryon asymmetry of the universe originates from the lepton asymmetry generated by the decay of right-handed neutrinos. In order to generate enough amount of baryon asymmetry via thermal leptogenesis, the reheating temperature is required to be higher than  $\sim 10^9$  GeV [76, 77]. Thus, for a viable scenario of thermal leptogenesis, scenarios realizing the gravitino mass of  $\mathcal{O}(10)$  TeV is suggested, like the pure gravity mediation scenario [65, 66, 67]. Notice that such a scenario works irrespective of the observational constraint on the  ${}^4\text{He}$  abundance, Eq. (2.3) or Eq. (2.4).

## 6 Conclusions and Discussion

We have revisited and updated the BBN constraints on long-lived particles. Compared with the previous analysis we have improved the following points. First, the SBBN reactions and their uncertainties are updated. Second, we have revised the hadronic shower calculation taking into account  $p \leftrightarrow n$  conversion in inelastic scatterings of energetic nucleons off the background  $p$  or  ${}^4\text{He}$ . Third, we have included the effects of the hadronic showers induced by the injections of energetic anti-nucleons ( $\bar{p}$  and  $\bar{n}$ ). Finally we have used the most recent observational data for the abundances of  ${}^4\text{He}$  and D and the cosmological parameters.

We have obtained the constraints on the abundance and lifetime of long-lived particles with various decay modes. They are shown in Figs. 12 and 13. The constraints become weaker when we include the  $p \leftrightarrow n$  conversion effects in inelastic scatterings because energetic neutrons change into protons and stop without causing hadrodissociations. On the other hand, inclusion of the energetic anti-nucleons makes the constraints more stringent. In addition, the recent precise measurement of the D abundance leads to stronger constraints. Thus, in total, the resultant constraints become more stringent than those obtained in the previous studies.

We have also applied our analysis to unstable gravitino. We have adopted several patterns of the mass spectrum of superparticles and derived constraints on the reheating temperature after inflation as shown in Fig. 16. The upper bound on the reheating temperature is  $\sim 10^5 - 10^6$  GeV for gravitino mass  $m_{3/2}$  less than a several TeV and  $\sim 10^9$  GeV for  $m_{3/2} \sim \mathcal{O}(10)$  TeV. This implies that the gravitino mass should be  $\sim \mathcal{O}(10)$  TeV for successful thermal leptogenesis.

In obtaining the constraints, we have adopted the observed  ${}^4\text{He}$  abundance given by Eq. (2.4) which is consistent with SBBN. On the other hand, if we adopt the other estimation (2.3),  ${}^4\text{He}$  abundance is inconsistent with SBBN. However, when long-lived particles with large hadronic branch have lifetime  $\tau_X \sim 0.1 - 100$  sec and abundance  $m_X Y_X \sim 10^{-9}$ , Eq. (2.3) becomes consistent with BBN.

In this work, we did not use  ${}^7\text{Li}$  in deriving the constraints since the plateau value in  ${}^7\text{Li}$  abundances observed in metal-poor stars (which had been considered as a primordial value)

---

density of the LSP. However, because the thermal relic abundance is strongly dependent on the MSSM parameters, we show the bound based on  $\Omega_{\text{LSP}}^{(\text{decay})}$ .

is smaller than the SBBN prediction by a factor 2–3 (lithium problem) and furthermore the recent discovery of much smaller  ${}^7\text{Li}$  abundances in very metal-poor stars cannot be explained by any known mechanism. However, the effects of the decaying particles on the  ${}^7\text{Li}$  and  ${}^6\text{Li}$  abundances are estimated in our numerical calculation. Interestingly, if we assume that the plateau value represents the primordial abundance, the decaying particles which mainly decays into  $e^+e^-$  can solve the lithium problem for  $\tau_X \sim 10^2 - 10^3$  sec and  $m_X Y_X \sim 10^{-7}$ .

## Acknowledgments

We thank Benjamin Fuks and Olivier Mattelaer for their supports in simulating gravitino decays with MadGraph5\_aMC@NLO. We thank Jens Chluba for useful discussions. This work was partially supported by JSPS KAKENHI Grant Nos. JP17H01131 (M.K. and K.K.), 17K05434 (M.K.), 26247042 (K.K.), 16H06490 (T.M.), and 26400239 (T.M.), and MEXT KAKENHI Grant Nos. JP15H05889 (M.K. and K.K.), and JP16H0877 (K.K.).

## References

- [1] D. Lindley, *Astrophys. J.* **294**, 1 (1985).
- [2] M. Y. Khlopov and A. D. Linde, *Phys. Lett.* **138B**, 265 (1984).
- [3] F. Balestra et al., *Sov. J. Nucl. Phys.* **39**, 626 (1984).
- [4] J. R. Ellis, J. E. Kim and D. V. Nanopoulos, *Phys. Lett.* **145B**, 181 (1984).
- [5] R. Juszkiewicz, J. Silk and A. Stebbins, *Phys. Lett.* **158B**, 463 (1985).
- [6] J. R. Ellis, D. V. Nanopoulos and S. Sarkar, *Nucl. Phys. B* **259**, 175 (1985).
- [7] J. Audouze, D. Lindley and J. Silk, *Astrophys. J.* **293**, L53 (1985).
- [8] D. Lindley, *Phys. Lett. B* **171**, 235 (1986).
- [9] M. Kawasaki and K. Sato, *Phys. Lett. B* **189**, 23 (1987).
- [10] R. J. Scherrer and M. S. Turner, *Astrophys. J.* **331**, 19 (1988).
- [11] J. R. Ellis, G. B. Gelmini, J. L. Lopez, D. V. Nanopoulos and S. Sarkar, *Nucl. Phys. B* **373**, 399 (1992).
- [12] M. Y. Khlopov, Y. L. Levitan, E. V. Sedelnikov and I. M. Sobol, *Phys. Atom. Nucl.* **57**, 1393 (1994) [*Yad. Fiz.* **57**, 1466 (1994)].
- [13] M. Kawasaki and T. Moroi, *Prog. Theor. Phys.* **93**, 879 (1995).

- [14] M. Kawasaki and T. Moroi, *Astrophys. J.* **452**, 506 (1995).
- [15] E. Holtmann, M. Kawasaki, K. Kohri and T. Moroi, *Phys. Rev. D* **60**, 023506 (1999).
- [16] K. Jedamzik, *Phys. Rev. Lett.* **84**, 3248 (2000).
- [17] M. Kawasaki, K. Kohri and T. Moroi, *Phys. Rev. D* **63**, 103502 (2001).
- [18] R. H. Cyburt, J. R. Ellis, B. D. Fields and K. A. Olive, *Phys. Rev. D* **67**, 103521 (2003).
- [19] M. Kusakabe et al., *Phys. Rev. D* **79**, 123513 (2009).
- [20] V. Poulin and P. D. Serpico, *Phys. Rev. D* **91**, no. 10, 103007 (2015).
- [21] M. H. Reno and D. Seckel, *Phys. Rev. D* **37**, 3441 (1988).
- [22] S. Dimopoulos, R. Esmailzadeh, L. J. Hall and G. D. Starkman, *Astrophys. J.* **330**, 545 (1988).
- [23] S. Dimopoulos, R. Esmailzadeh, L. J. Hall and G. D. Starkman, *Phys. Rev. Lett.* **60**, 7 (1988).
- [24] S. Dimopoulos, R. Esmailzadeh, L. J. Hall and G. D. Starkman, *Nucl. Phys. B* **311**, 699 (1989).
- [25] K. Kohri, *Phys. Rev. D* **64**, 043515 (2001).
- [26] K. Jedamzik, *Phys. Rev. D* **70**, 063524 (2004).
- [27] M. Kawasaki, K. Kohri and T. Moroi, *Phys. Lett. B* **625**, 7 (2005).
- [28] M. Kawasaki, K. Kohri and T. Moroi, *Phys. Rev. D* **71**, 083502 (2005).
- [29] K. Kohri, T. Moroi and A. Yotsuyanagi, *Phys. Rev. D* **73**, 123511 (2006).
- [30] K. Jedamzik, *Phys. Rev. D* **74**, 103509 (2006).
- [31] M. Kawasaki, K. Kohri, T. Moroi and A. Yotsuyanagi, *Phys. Rev. D* **78**, 065011 (2008).
- [32] R. H. Cyburt, J. Ellis, B. D. Fields, F. Luo, K. A. Olive and V. C. Spanos, *JCAP* **0910**, 021 (2009).
- [33] S. Weinberg, *Phys. Rev. Lett.* **48**, 1303 (1982).
- [34] M. Kawasaki, K. Kohri, T. Moroi and Y. Takaesu, *Phys. Lett. B* **751**, 246 (2015).
- [35] R. Cooke, M. Pettini, R. A. Jorgenson, M. T. Murphy and C. C. Steidel, *Astrophys. J.* **781**, no. 1, 31 (2014).

- [36] G. Sigl, K. Jedamzik, D. N. Schramm and V. S. Berezinsky, *Phys. Rev. D* **52**, 6682 (1995).
- [37] J. Geiss and G. Gloeckler, *Space Science Reviews* **106**, 3 (2003).
- [38] Y. I. Izotov, T. X. Thuan and N. G. Guseva, *Mon. Not. Roy. Astron. Soc.* **445**, 778 (2014).
- [39] E. Aver, K. A. Olive and E. D. Skillman, *JCAP* **1507**, no. 07, 011 (2015).
- [40] L. Sbordone, P. Bonifacio, E. Caffau, H.-G. Ludwig, N. T. Behara, J. I. G. Hernandez, M. Steffen and R. Cayrel *et al.*, *Astron. Astrophys.* **522**, A26 (2010).
- [41] P. A. R. Ade *et al.* [Planck Collaboration], *Astron. Astrophys.* **594**, A13 (2016).
- [42] T. Sjostrand *et al.*, *Comput. Phys. Commun.* **191**, 159 (2015).
- [43] P. D. Serpico, S. Esposito, F. Iocco, G. Mangano, G. Miele and O. Pisanti, *JCAP* **0412**, 010 (2004).
- [44] R. H. Cyburt and B. Davids, *Phys. Rev. C* **78**, 064614 (2008).
- [45] J. P. Meyer, *Astron. Astrophys. Suppl.* **7** 417 (1972).
- [46] C. Patrignani *et al.* [Particle Data Group], *Chin. Phys. C* **40**, no. 10, 100001 (2016).
- [47] E. Bracci, J. P. Droulez, E. Flaminio, J. D. Hansen, D. R. O. Morrison, and Douglas Robert Ogston, CERN-HERA-73-1 (1973).
- [48] J. Hisano, M. Kawasaki, K. Kohri, T. Moroi and K. Nakayama, *Phys. Rev. D* **79**, 083522 (2009).
- [49] R. J. Scherrer, J. M. Cline, S. Raby and D. Seckel, *Phys. Rev. D* **44**, 3760 (1991).
- [50] W. Hu and J. Silk, *Phys. Rev. Lett.* **70**, 2661 (1993).
- [51] J. Chluba and R. A. Sunyaev, *Mon. Not. Roy. Astron. Soc.* **419**, 1294 (2012).
- [52] J. Chluba, *Mon. Not. Roy. Astron. Soc.* **436**, 2232 (2013).
- [53] D. J. Fixsen, E. S. Cheng, J. M. Gales, J. C. Mather, R. A. Shafer and E. L. Wright, *Astrophys. J.* **473**, 576 (1996).
- [54] J. Chluba and D. Jeong, *Mon. Not. Roy. Astron. Soc.* **438**, no. 3, 2065 (2014).
- [55] E. Dimastrogiovanni, L. M. Krauss and J. Chluba, *Phys. Rev. D* **94**, no. 2, 023518 (2016).
- [56] K. Ishiwata, M. Kawasaki, K. Kohri and T. Moroi, *Phys. Lett. B* **689**, 163 (2010).

- [57] M. Endo, K. Hamaguchi and F. Takahashi, Phys. Rev. Lett. **96**, 211301 (2006).
- [58] S. Nakamura and M. Yamaguchi, Phys. Lett. B **638**, 389 (2006).
- [59] M. Kawasaki, F. Takahashi and T. T. Yanagida, Phys. Lett. B **638**, 8 (2006).
- [60] M. Bolz, A. Brandenburg and W. Buchmuller, Nucl. Phys. B **606**, 518 (2001) Erratum: [Nucl. Phys. B **790**, 336 (2008)].
- [61] J. Pradler and F. D. Steffen, Phys. Rev. D **75**, 023509 (2007).
- [62] V. S. Rychkov and A. Strumia, Phys. Rev. D **75**, 075011 (2007).
- [63] J. Ellis, M. A. G. Garcia, D. V. Nanopoulos, K. A. Olive and M. Peloso, JCAP **1603**, no. 03, 008 (2016).
- [64] S. P. Martin, Adv. Ser. Direct. High Energy Phys. **21**, 1 (2010) [Adv. Ser. Direct. High Energy Phys. **18**, 1 (1998)].
- [65] M. Ibe, T. Moroi and T. T. Yanagida, Phys. Lett. B **644**, 355 (2007).
- [66] M. Ibe and T. T. Yanagida, Phys. Lett. B **709**, 374 (2012).
- [67] N. Arkani-Hamed, A. Gupta, D. E. Kaplan, N. Weiner and T. Zorawski, arXiv:1212.6971 [hep-ph].
- [68] L. Randall and R. Sundrum, Nucl. Phys. B **557**, 79 (1999).
- [69] G. F. Giudice, M. A. Luty, H. Murayama and R. Rattazzi, JHEP **9812**, 027 (1998).
- [70] J. Alwall *et al.*, JHEP **1407**, 079 (2014).
- [71] C. Duhr and B. Fuks, Comput. Phys. Commun. **182**, 2404 (2011).
- [72] C. Degrande, C. Duhr, B. Fuks, D. Grellscheid, O. Mattelaer and T. Reiter, Comput. Phys. Commun. **183**, 1201 (2012).
- [73] N. D. Christensen *et al.*, Eur. Phys. J. C **73**, no. 10, 2580 (2013).
- [74] A. Alloul, N. D. Christensen, C. Degrande, C. Duhr and B. Fuks, Comput. Phys. Commun. **185**, 2250 (2014).
- [75] M. Fukugita and T. Yanagida, Phys. Lett. B **174**, 45 (1986).
- [76] G. F. Giudice, A. Notari, M. Raidal, A. Riotto and A. Strumia, Nucl. Phys. B **685**, 89 (2004).
- [77] W. Buchmuller, P. Di Bari and M. Plumacher, Annals Phys. **315**, 305 (2005).